UNIVERSITY OF OKLAHOMA

GRADUATE COLLEGE

FAST TEMPERATURE-FIELD PREDICTION IN WIRE-ARC ADDITIVE MANUFACTURING USING FUNCTIONAL MODELS AND NEURAL NETWORKS

A THESIS

SUBMITTED TO THE GRADUATE FACULTY

in partial fulfillment of the requirements for the

Degree of

MASTER OF SCIENCE

By

ALI DASHTI RAHMATABADI

Norman, Oklahoma

2025

FAST TEMPERATURE-FIELD PREDICTION IN WIRE-ARC ADDITIVE MANUFACTURING USING FUNCTIONAL MODELS AND NEURAL NETWORKS

A THESIS APPROVED FOR THE
SCHOOL OF INDUSTRIAL AND SYSTEMS ENGINEERING

BY THE COMMITTEE CONSISTING OF

Dr. Cesar Ruiz (Chair)

Dr. Janet K. Allen

Dr. Shuozhi Xu

Acknowledgments

I would like to express my deepest gratitude to Dr. Cesar Ruiz for his unwavering guidance and support throughout my academic journey. I am also sincerely thankful to the faculty and staff at the School of Industrial and Systems Engineering at the University of Oklahoma for their valuable insights and encouragement.

Lastly, to my dear family and friends: your love, patience, and unwavering belief in me have been the quiet strength behind every step I have taken, and I am endlessly grateful for you.

Table of Contents

List Of Tables

List Of Figures

Table 1: List of abbreviations used in this thesis

Abbreviation	Full term
AM	Additive Manufacturing
APDL	ANSYS Parametric Design Language
BC	Between-Cluster
ConvLSTM	Convolutional Long Short-Term Memory Network
CNN	Convolutional Neural Network
DDPG	Deep Deterministic Policy Gradient
DeepONet–RNN	Deep Operator Network – Recurrent Neural Network
DED	Directed Energy Deposition
FEM	Finite Element Method
GP	Gaussian Process
GMAW	Gas Metal Arc Welding
GRU	Gated Recurrent Unit
GTAW	Gas Tungsten Arc Welding
LSTM	Long Short-Term Memory
MARE	Mean Absolute Relative Error
MAM	Metal Additive Manufacturing
ML	Machine Learning
MLP	Multilayer Perceptron
MSE	Mean Squared Error
PAW	Plasma Arc Welding
PBF	Powder Bed Fusion
PINN	Physics-Informed Neural Network
RNN	Recurrent Neural Network
SVR	Support Vector Regression
TPE	Tree-Structured Parzen Estimator
WAAM	Wire Arc Additive Manufacturing
WP	Within-Power

Abstract

Wire-based metal additive manufacturing is a promising technique for fabricating large-scale structural components across various industrial sectors. Using robot-assisted deposition, these technologies offer relatively low equipment cost for fast fabrication on large areas. However, high operating temperatures and heat accumulation create significant thermal stresses, causing distortion and roughness in deposited layers. Precise thermal history prediction is essential for achieving proper deposition process planning and control. Typically, finite element method (FEM) simulations are used to solve large PDEs for thermal analysis. However, these methods are computationally prohibitive for large parts, making them unsuited the effective automation of the deposition process. In this paper, we develop a functional regression and neural network model as surrogates for thermal history prediction during single layer, single track deposition. We studied the effect of track geometry on the FEM results, the accuracy of the proposed surrogate methodology for predictions of the thermal history profile for each geometry and discuss its applicability to help automate process planning and control in large-scale metal additive manufacturing.

Chapter 1

Introduction

1.1 Background and Motivation

Additive manufacturing (AM) has emerged as a practical approach in modern manufacturing by enabling the layer-by-layer fabrication of complex parts with reduced material waste and shorter lead times. Among the various AM techniques, wire-based metal additive manufacturing (MAM), particularly Wire Arc Additive Manufacturing (WAAM), has gained attention due to its high deposition rates, and suitability for fabrication of large components. These characteristics make WAAM attractive for sectors such as aerospace, shipbuilding, automotive, and energy (Chen et al. 2024), where part size, customization, and mechanical performance are important.

In WAAM, the material is deposited using an electric arc as a heat source that melts the wire feedstock and forms a moving molten pool. As the torch advances, the pool solidifies and previously deposited material is reheated by subsequent passes and layers. The resulting temperature field is strongly time-dependent and non-uniform in space, influenced by process parameters, path geometry, and the thermal properties of the substrate and deposited material (Chen et al. 2024; Norrish et al. 2021). This thermal behavior is closely linked to many aspects of part quality, including geometry, microstructure, and residual stress.

In this work, the term thermal history means the temperature of the part as a function of time at different points in the build. Knowing how the temperature changes

at these locations is useful, because it summarizes how heat is deposited and removed during deposition. Once this information is available, it can be reused by other models, for example for estimating distortion or assessing process stability. In this thesis, we focus on predicting these thermal histories for single-layer, single-track WAAM on two representative geometries: a linear path and a half-circular path.

1.2 Problem Statement

Although WAAM offers high deposition rates and scalability, its thermal behavior creates several practical challenges. First, the combination of high heat input, repeated thermal cycling, and large build dimensions can lead to the accumulation of thermal stresses and distortions in large-scale parts. As the bead length and overall component size increase, local variations in temperature can accumulate and manifest as warping, loss of dimensional accuracy, or the need for extensive post-processing. Predicting the thermal history throughout the build is therefore important for anticipating these effects and for identifying process settings that mitigate them.

Second, finite element method (FEM) simulations are commonly used to study heat transfer in WAAM because they solve the governing heat-conduction equations with high fidelity (Yan et al. 2018). However, detailed transient thermal analyses are computationally intensive, especially when fine spatial and temporal resolution is required near the melt pool. Simulations that are feasible for short tracks or a small number of parameter settings become expensive when extended to longer paths, multiple power levels, or systematic parameter studies. This computational cost limits the use of FEM-based thermal predictions in situations where many alternatives must be evaluated or where near–real-time feedback would be desirable.

Third, when developing surrogate models to approximate thermal histories, there is a trade-off between interpretability and flexibility. Functional models with carefully chosen basis functions and spatially varying coefficients can reflect aspects of the underlying physics and provide insight into how time, power, and spatial location influence the temperature field. At the same time, they may not capture all nonlinear interactions present in complex datasets. Neural network models, in contrast, can represent highly nonlinear relationships and adapt to complex patterns in simulated data, but they are typically less transparent and require careful design to generalize outside the training conditions. This thesis is motivated by the need to evaluate these trade-offs in the specific context of WAAM thermal prediction and to develop surrogate models that are both accurate and computationally efficient.

The next section formulates the research objectives that guide the development and comparison of functional and neural surrogate models in this work.

1.3 Research Objectives

The issues outlined in the previous section motivate the use of surrogate models to predict thermal histories in WAAM more efficiently, while still retaining useful structure and interpretability. The overall goal of this thesis is to develop and compare two such surrogate models for single-layer, single-track WAAM on representative geometries. The specific research objectives are as follows:

1. **Simulation of WAAM deposition for linear and half-circular geometries.** Design two single-track geometries, a straight linear path and a half-circular path, and use ANSYS transient thermal analysis to simulate WAAM deposition on each. The simulations should incorporate a cluster-based activation strategy and a dense layout of virtual probes so that the resulting dataset

captures longitudinal and cross-sectional temperature variations across multiple power levels.

2. **Development of a functional model with spatially varying coefficients.** Formulate and implement a functional regression model that represents the logarithm of temperature as a function of time, power level, and spatial location. Use tensor-product basis functions and spatially varying coefficients to capture cluster-to-cluster variation and cross-sectional heterogeneity, and fit the model to the simulated thermal histories.

3. **Development of a neural network model for thermal history prediction.** Construct a neural network surrogate that uses process parameters such as, time, power, path coordinate, cluster index, and cross-sectional coordinates to predict the logarithm of temperature at probe locations. Design the network architecture, training procedure, and hyperparameter tuning strategy so that it can learn complex patterns present in the simulation data.

4. **Comparison of functional and neural models in terms of accuracy and efficiency.** Evaluate both surrogate models on held-out data for linear and half-circular geometries and for different types of test sets. Compare their performance using the Mean Absolute Relative Error (MARE) and related metrics across heating, rapid cooling, and cooling phases, and assess their computational cost for training and prediction.

These objectives guide the methodology and analysis presented in the subsequent chapters, where the simulation framework, functional model, and neural network model are developed and evaluated in detail.

1.4 Thesis Organization

This thesis is organized into six main chapters. Chapter 1 introduces the background and motivation for studying thermal histories in WAAM, states the main problems addressed in this work, and formulates the research objectives. Chapter 2 reviews the relevant literature. It summarizes the thermal physics of WAAM, discusses finite element methods and heat source models used for thermal analysis, and surveys existing surrogate modeling approaches, including machine learning techniques and functional data analysis methods that are related to this study. Chapter 3 describes the data generation process. It presents the linear and half-circular geometries, explains the Python and CadQuery workflow used to build the CAD models, and details the ANSYS transient thermal simulation setup. Chapter 4 outlines the methodology for surrogate modeling. It first introduces the functional modeling framework, including the representation of the logarithm of temperature using tensor-product basis functions and spatially varying coefficients. It then presents the neural network modeling approach, describing the choice of input features, network architecture, training strategy, and hyperparameter tuning procedure. Together, these sections define the two surrogate models that are later compared. Chapter 5 presents the results and comparative discussion. It reports performance metrics, including Mean Absolute Relative Error (MARE), for both the functional model and the neural network on different test sets and thermal phases. The chapter compares accuracy and computational efficiency, examines error patterns for linear and half-circular geometries, and discusses how these patterns relate to the underlying thermal behavior. Lastly, Chapter 6 concludes the thesis. It summarizes the main findings, highlights the contributions of the work, and discusses possible extensions, including multi-layer deposition, additional geometries, and integration with models for geometry, microstructure, or residual stress.

Chapter 2

Literature review

2.1 Fundamentals of WAAM

WAAM is a wire-fed directed energy deposition (DED) process that uses welding technology to fabricate metal parts layer by layer. It has emerged as a prominent solution within metal AM due to its ability to manufacture large-scale, near-net-shape components efficiently and at relatively low cost (Jafari et al. 2021). According to this study, key factors of WAAM also showed as 2.1. Compared with powder bed fusion (PBF) processes, WAAM offers higher deposition rates, larger build envelopes, and reduced material cost, primarily because wire feedstock is cheaper and easier to handle than metal powder Dekis et al. (2025).

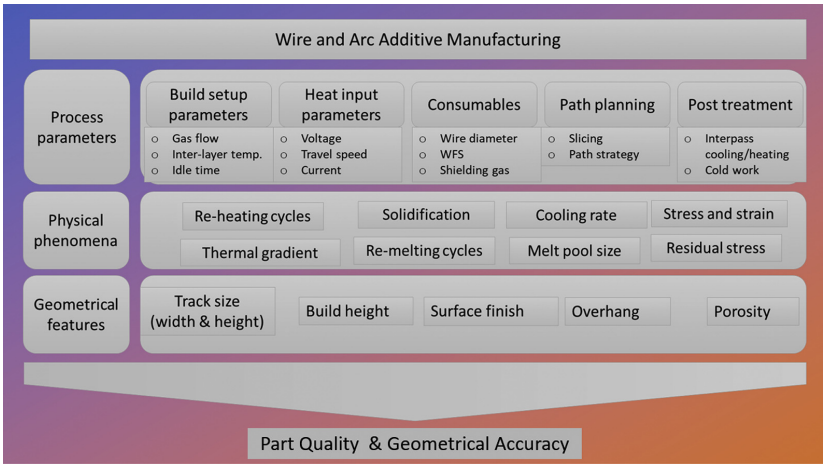

Figure 2.1: Schematic representation of the key factors governing wire and arc AM (Jafari et al. 2021)

In WAAM, a metallic wire is melted by an electric arc and deposited onto a substrate or previously deposited layers, as illustrated in Figure 2.2. The main process variants include Gas Metal Arc Welding (GMAW), Gas Tungsten Arc Welding (GTAW), and Plasma Arc Welding (PAW). GMAW-based WAAM is the most frequently used configuration due to its higher deposition rates and process efficiency, while GTAW and PAW are often preferred when improved precision, lower spatter, or better surface finish are required Lambiase et al. (2025).

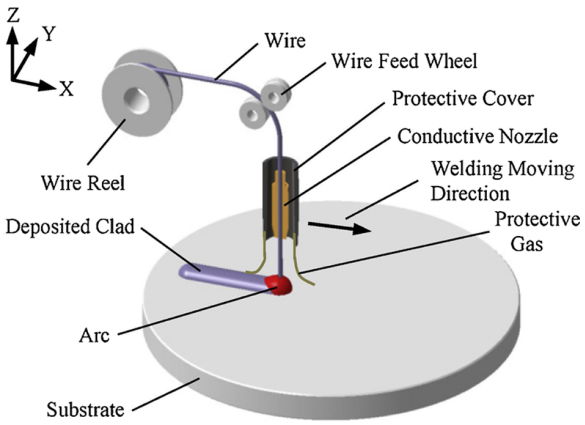

Figure 2.2: Gas metal arc welding-based AM process (Zhou et al. 2021).

WAAM offers several important advantages over conventional subtractive manufacturing and some powder-based AM technologies. It provides high material utilization, shorter lead times, and reduced waste, making it attractive for high-value alloys such as titanium, nickel-based alloys, and specialized steels commonly used in aerospace, marine, and automotive applications (Zhang et al. 2024). Typical deposition rates in the range of 1–10 kg/h enable rapid production of medium- to large-scale components that would be difficult or uneconomical to produce using traditional methods (Jafari et al. 2021; Dekis et al. 2025).

Despite these benefits, WAAM is associated with several challenges, most of which are linked to its thermal behavior. The high heat input and repeated thermal cycling

can generate significant residual stresses, geometric distortion, and complex microstructural variations, as illustrated in Figure 2.3. Non-uniform thermal gradients and rapid cooling rates may lead to warping, loss of dimensional accuracy, or cracking, ultimately affecting the structural integrity of the final component (Zhang et al. 2024). Effective heat management such as, through optimized inter-pass cooling, active cooling, or localized heating is therefore essential to maintain dimensional stability and reduce defect occurrence (Jafari et al. 2021).

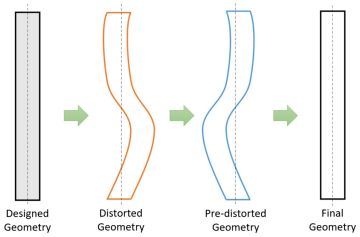

(a) Geometric distortion Afazov et al. (2021).

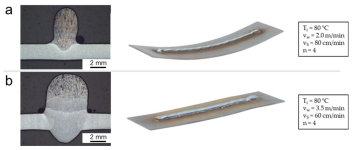

(b) Delamination Wacker et al. (2021).

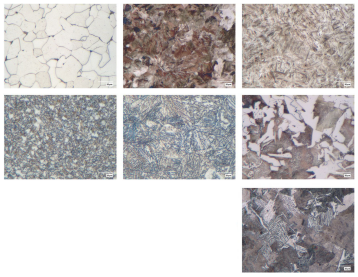

(c) Microstructural defects Schneider et al. (2024).

Figure 2.3: Illustration of common WAAM-induced defects.

Microstructural evolution in WAAM is strongly influenced by process parameters such as current, voltage, travel speed, wire feed rate, and interlayer temperature. These parameters determine cooling rates and thermal gradients, which in turn affect grain size, phase distribution, and mechanical properties of the deposited material (Lambiase et al. 2025; Zhang et al. 2024). Consequently, careful selection and optimization of process parameters are required to obtain consistent component quality. In addition, defects such as porosity, lack of fusion, and inclusions must be mitigated through appropriate process planning (Singh et al. 2021), material selection (Wahsh et al. 2018), and monitoring strategies (Xia et al. 2020).

Overall, WAAM presents significant potential for industrial manufacturing of large and complex metallic components, but its widespread adoption depends on addressing

these thermally driven challenges. A detailed understanding of the relationship between process parameters, thermal history, and part quality is therefore essential. The next sections focus on modeling approaches that aim to describe and predict the WAAM thermal field, with particular emphasis on finite element methods and surrogate models for fast thermal history prediction.

2.2 Finite Element Thermal Modelling for WAAM

Finite element method (FEM) is widely used to analyze heat transfer and thermo-mechanical behaviour in WAAM and related welding processes. It provides a way to resolve the temperature field in space and time under realistic boundary conditions and process parameters, and is often treated as a reference tool (Sampaio et al. 2023; Chen et al. 2024; Love et al. 2025).

2.2.1 Governing equations and modelling assumptions

Thermal analyses in WAAM typically start from the transient heat conduction equation with internal heat generation (Pina and Fernandes 1984),

$$\rho c_p \frac{\partial T}{\partial t} = \nabla \cdot (k \nabla T) + Q, \tag{2.1}$$

where T is temperature, ρ is density, c_p is specific heat, k is thermal conductivity, and Q represents the volumetric heat input from the arc. The equation is solved over a three-dimensional domain that includes the substrate and the deposited material, subject to initial and boundary conditions that describe heat loss through conduction to fixtures, convection to the surrounding gas, and radiation to the environment.

In this work, Eq. (2.1) is interpreted as a pointwise energy balance, and all material properties are treated as temperature-dependent fields, i.e., $\rho(T)$, $c_p(T)$, and $k(T)$. These assumptions replace the use of bulk-averaged properties and ensure that the governing equation reflects the local thermophysical behavior encountered in WAAM.

To keep the problem tractable, several simplifications are usually adopted. Fluid flow in the molten pool is often neglected or approximated through an effective thermal conductivity. Latent heat during melting and solidification can be included by modifying the specific heat over the phase-change interval or by adding an additional source term. Material properties are generally taken as temperature-dependent and sometimes differ between the substrate and deposited material Chen et al. (2024); Love et al. (2025). For thermo-mechanical analyses, the thermal solution is coupled to elastic–plastic constitutive models that include thermal expansion and temperature-dependent yield strength.

2.2.2 Heat source models and element activation

A central aspect of FEM for WAAM is the representation of the moving heat source. Common models, as shown in Fig. 2.4, include surface or volumetric Gaussian distributions (Teixeira et al. 2014), double-ellipsoidal Goldak-type heat sources (Goldak et al. 1984), and variants tailored to specific arc configurations (Nascimento et al. 2023). These formulations prescribe the spatial distribution of the volumetric term Q in the heat equation and are calibrated against experimentally observed melt-pool dimensions, peak temperatures, and fusion boundaries. The symbols used in these heat-source descriptions, such as a, b, c_f, c_r, r_0, and q_0'', control the transverse width, penetration depth, longitudinal extent, and peak intensity of the applied heat flux are defined in Table 2.1.

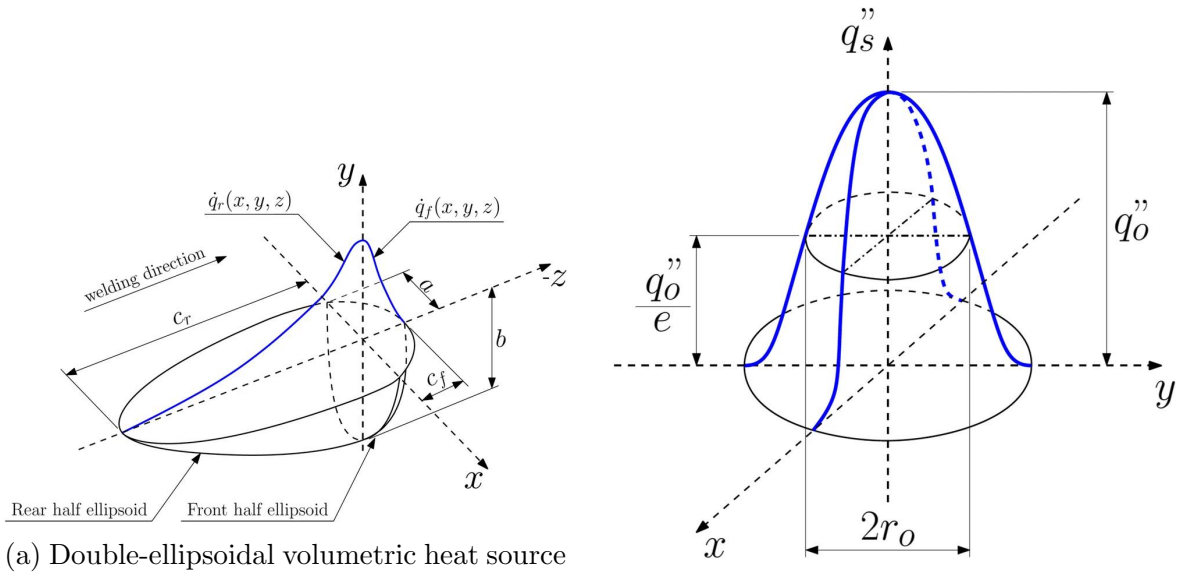

(a) Double-ellipsoidal volumetric heat source (Goldak-type).

(b) Gaussian surface heat flux source.

Figure 2.4: Comparison of common heat source representations used in thermal FEM models for welding and WAAM. Lin et al. (2025)

Table 2.1: Definition of parameters used in common WAAM heat-source models.

Symbol	**Meaning**
a	Semi-axis in transverse (x) direction; heat-source half-width
b	Semi-axis in depth (z) direction; penetration depth
c_f	Semi-axis of the front ellipsoid along travel direction (y)
c_r	Semi-axis of the rear ellipsoid along travel direction (y)
$\dot{q}_f(x,y,z)$	Volumetric heat flux density in the front ellipsoid
$\dot{q}_r(x,y,z)$	Volumetric heat flux density in the rear ellipsoid
r_0	Characteristic Gaussian radius of surface heat flux
q_0''	Peak surface heat flux at beam/arc center
e	Process efficiency factor (absorbed fraction of power)

The motion of the torch along the toolpath is implemented by translating the heat source in time according to the programmed travel speed. In single-track simulations, this is achieved by updating the source position at each time step along a predefined

path; multi-layer builds require additional passes and path patterns. To account for the progressive addition of material, many WAAM models use element birth-and-death techniques: elements representing future deposited material are initially deactivated and subsequently activated when the heat source reaches their region. This strategy allows the geometry to evolve without remeshing, while still capturing heat conduction through the growing wall or bead (Schoinochoritis et al. 2017).

2.2.3 Applications and limitations

FEM has been applied to a wide range of WAAM scenarios, including single beads on plate, multi-layer walls, and more complex demonstrator components (Barath Kumar and Manikandan 2022). These studies have been used to investigate the influence of power, travel speed, and inter-pass time on temperature gradients and cooling rates, to predict residual stresses and distortion, and to compare different deposition strategies. In many studies, the FEM predictions have been validated against thermocouple (Xiong et al. 2017) and infrared camera (Bai et al. 2013) measurements, showing similar results once the heat source parameters and thermal boundary conditions are properly calibrated.

However, high-fidelity FEM comes with significant computational cost and other challenges as brought in 2.5. Three-dimensional transient simulations with fine spatial and temporal resolution can require hours of computation for a single parameter set, especially when thermo-mechanical coupling is included. Exploring multiple power levels, path variants, or dwell times quickly becomes expensive, and full-scale industrial components may be beyond reach with standard resources.

These limitations motivate the use of FEM not as a tool for exhaustive parameter search, but as a generator of high-quality reference data. By running a carefully chosen

set of simulations and recording temperature histories at many locations, one can construct a database that supports the development of surrogate models. The remainder of this chapter reviews such surrogate approaches, including neural network models and functional data analysis, which aim to reproduce FEM-level thermal predictions at a much lower computational cost.

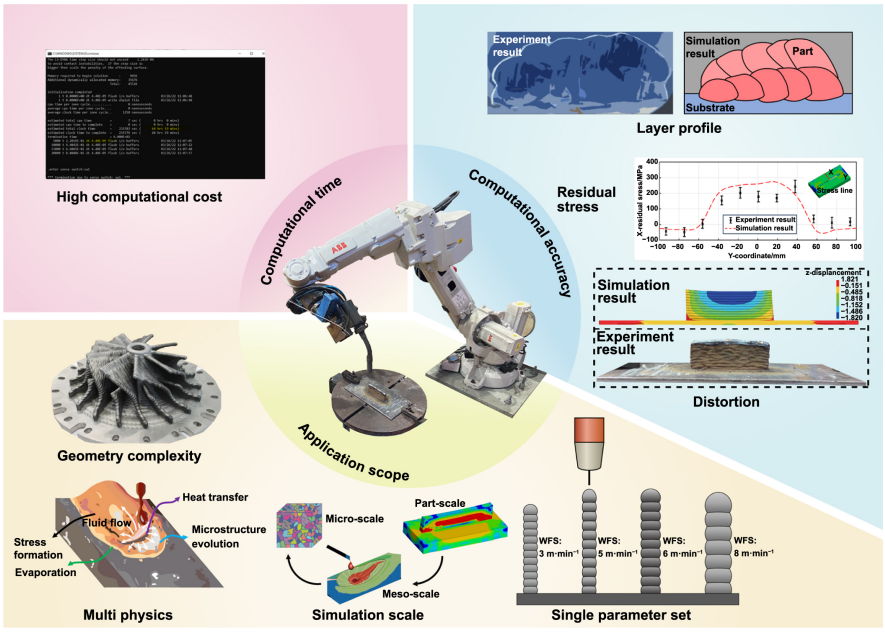

Figure 2.5: Summary of challenges to the simulation in WAAM (Chen et al. 2024).

2.3 Data-driven surrogate models in metal AM and WAAM

Data-driven surrogate models have become an important alternative to finite element methods simulations for predicting thermal and thermo-mechanical responses in MAM. To reduce computational burden, machine learning (ML) techniques such as neural networks and regression models have been extensively studied for thermal prediction and process monitoring. Mozaffar et al. (2018) utilized recurrent neural networks (RNNs)

with gated recurrent units (GRUs) to predict high-dimensional thermal histories in directed energy deposition, taking as input features that describe laser power, scan speed, spatial location, and neighborhood geometry. Their results showed that deep sequence models can reproduce multi-layer thermal histories at substantially lower cost than repeated FE simulations. Thien et al. (2024) examined the capability of multi-layer perceptron (MLP), autoregressive integrated moving average, and long short-term memory (LSTM) models for forecasting WAAM process instabilities from historical data streams, highlighting how data-driven models can anticipate process deviations before they manifest in part quality. Nalajam and Varadarajan (2021) proposed a hybrid CNN–LSTM deep learning model to forecast melt pool temperatures while exploiting spatio-temporal correlations, and demonstrated improved prediction accuracy over purely temporal or purely spatial baselines.

More recent studies have started to couple thermal and mechanical responses and to embed physical constraints directly into the surrogate model. A representative example is the physics-informed neural operator for real-time distortion prediction in metallic AM (Tian et al. 2025). As shown in Figure 2.6, temperature and distortion fields from a calibrated thermo-mechanical WAAM model are used to train several surrogates, including a CNN, a spatio-temporal Convolutional Long Short-Term Memory Network (ConvLSTM), a Deep Operator Network – Recurrent Neural Network (DeepONet–RNN), and a physics-informed DeepONet–RNN that incorporates the heat-conduction equation into the loss function. The physics-informed model achieves the best long-horizon distortion prediction accuracy while keeping prediction times in the millisecond range, illustrating how embedding governing equations can reduce error accumulation and improve generalization under varying process parameters.

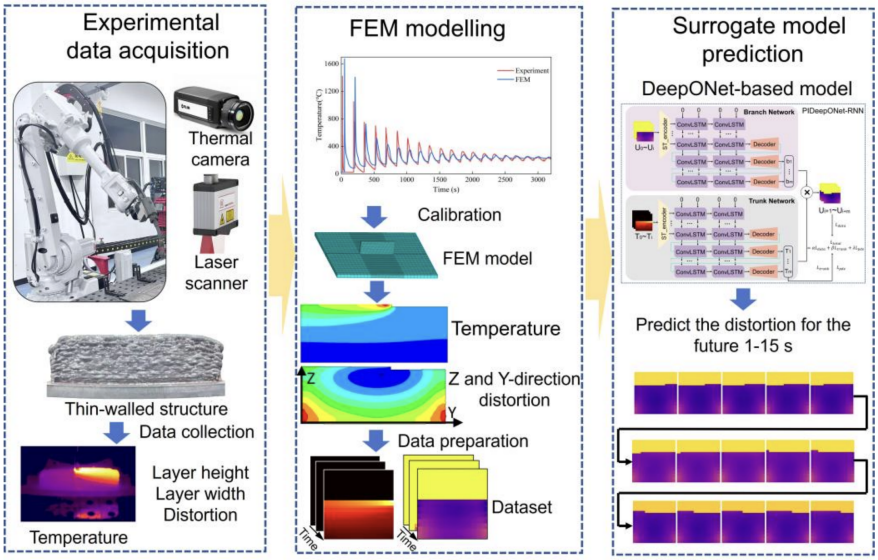

Figure 2.6: Overall framework of a real-time distortion prediction system in metallic AM based on physics-informed neural operators Tian et al. (2025).

Within WAAM specifically, several data-driven models have been proposed for process–property and process–geometry relationships. In Barik et al. (2024), process parameters for ER70S-6 WAAM (current, voltage, and travel speed) were optimized using a response surface method, and a support vector regression (SVR) model was trained to predict tensile properties and microstructural characteristics of the deposited material. The study showed that an SVR surrogate can capture the nonlinear dependence of mechanical properties on process settings and can be used to explore parameter combinations beyond those tested experimentally. For 17-4PH stainless steel WAAM, Irfan et al. (2025) combined a backpropagation neural network with a genetic algorithm to relate wire feed rate, torch travel speed, and gas flow rate to bead geometry. The optimized model achieved a strong correlation between predicted and measured bead dimensions and was used to identify parameter sets that improve bead uniformity and deposition efficiency.

Dynamic modelling and data-driven control have also been investigated. In Mattera et al. (2025b), experimental GMA-AM data were used to develop time-dependent

process models with several state-of-the-art techniques, and ensemble strategies were applied to combine individual model predictions. A simple averaging ensemble reduced the mean absolute error, while a reinforcement-learning-based ensemble achieved further improvements and was demonstrated in an anomaly-detection application for process monitoring. Reinforcement learning has been studied more directly for WAAM control (Mattera et al. 2025a), where a reduced-order model identified from experimental data was used to train a Deep Deterministic Policy Gradient (DDPG) controller. The trained controller generated actions to produce a target geometry, and the study emphasized the importance of a realistic WAAM simulator for sim-to-real transfer of the learned policy.

From a quality assurance perspective, artificial intelligence has been widely explored for defect-related indicators. The review by Mondal and Goswami (2024) surveys the use of convolutional neural networks for defect detection, support vector machines for classification of material properties, and reinforcement learning for real-time process optimization in AM. The authors discuss how large datasets from in-situ sensors and monitoring systems can be used to detect porosity, lack of fusion, and other defects, and they highlight challenges related to data preprocessing, model interpretability, and integration with existing AM systems.

Physics-informed neural networks have been proposed as an alternative to purely data-driven surrogates for thermal fields in large-scale directed energy deposition. In Ryan et al. (2025), a PINN framework for wire-arc DED was developed by enforcing the governing heat equation at collocation points in space and time rather than relying solely on data from FEM simulations or experiments. By carefully designing the sampling of collocation points, the authors showed that the PINN can approximate the thermal field of thick walls and plates with substantial reductions in computational cost

compared to conventional FEM, while maintaining the desired accuracy and offering super-resolution capabilities in regions of interest.

The main drawback of many ML-based surrogates is the need for extensive training datasets and the limited applicability to new geometries or process conditions that differ from those represented in the training data. In addition, ML-based predictions often lack physical interpretability, making it difficult to extract insights about how specific process variables influence the thermal history. To address these shortcomings, this thesis combines two complementary surrogate modeling approaches for single-layer single-track WAAM.

2.4 Assumptions

This study relies on a set of modeling assumptions that define the scope of FEM and the process conditions under which the surrogate models are developed. The following subsections summarize the key physical, numerical and process-related assumptions that underpin the results.

2.4.1 Physical and FEM Assumptions

The FEM assume that both the deposited WAAM bead and the base plate exhibit isotropic thermal behavior. Although the governing equation is written in a general form, the thermal conductivity is treated as a scalar quantity, and directional dependence of heat conduction is not considered. For the deposited material, 316L stainless steel, density, specific heat, and thermal conductivity are modeled as temperature-dependent and are taken from the ANSYS material library without additional experimental calibration or uncertainty quantification. The base plate is modeled as structural steel with fixed properties, and the interface between the bead and the base

plate is assumed to be perfectly bonded, without explicit modeling of thermal contact resistance or imperfect adhesion.

Heat losses from all exposed surfaces are represented using a combined convection–radiation boundary condition. A constant emissivity at 0.9 is assigned to the metallic surfaces, the ambient temperature is fixed at 25 ℃, and a uniform convective heat transfer coefficient is applied over all boundaries. Spatial and temporal variations in gas flow, shielding effects, or ambient conditions are not modeled, and the environment is treated as homogeneous. The arc heat input is represented by a Gaussian volumetric heat source with fixed geometric parameters that define its effective radius and penetration. Electrical input power is converted to thermal power using a constant process efficiency factor of 0.85 for all simulations and power levels. The analysis is purely thermal and mechanical effects such as residual stress, distortion, and plastic deformation are not coupled back into the thermal model and are assumed not to substantially alter the heat transfer behavior within the simulated time window.

2.4.2 Geometric and Process Assumptions

The WAAM setup is modeled with idealized but fixed geometric dimensions. The base plate has prescribed length, width, and thickness, and the deposited bead is assigned a nominal cross-section with constant width and height along the entire deposition path. Variations in bead geometry arising from local temperature changes, curvature effects, or gravitational sagging are not explicitly represented; instead, the bead shape corresponds to a uniform track. The torch is assumed to follow the prescribed path with perfect accuracy, without positional deviation or oscillation.

Process parameters are held constant throughout each simulation. The torch travel speed is fixed at a specified value, and the wire feed rate and resulting deposition rate remain constant along the track. Power levels are applied as constant values rather

than being modulated or ramped, and short-term arc fluctuations or metal transfer dynamics are not modeled. The ambient temperature is taken as uniform, and no active cooling, preheating, or additional thermal management strategies are included beyond the specified boundary conditions. Together, these assumptions define an idealized and repeatable WAAM process in which geometric variability and process disturbances are intentionally suppressed to isolate the effects of power input, path geometry, and material properties on the resulting thermal history.

Chapter 3

FEM-Based Thermal Simulation

3.1 Overview of FEM Approach in ANSYS

FEM simulation provides a robust framework for analyzing the complex thermal behavior associated with wire-based AM processes. In this study, FEM was employed to model the heat transfer dynamics of single-layer, single-track WAAM deposition using the ANSYS Workbench R2 2024 suite, specifically the AM DED module, running on Dell Pro Max Micro FCM2250 computer. The primary goal of the FEM setup was to generate high-fidelity temperature data that could serve both as a ground truth for evaluating surrogate model accuracy and as training data for the model itself.

The simulation workflow consisted of three main stages: (1) geometric modeling of the base plate and deposited track, (2) meshing and temporal segmentation of the track into discrete deposition clusters, and (3) transient thermal analysis incorporating realistic process parameters and boundary conditions. The FEM model integrated both the thermal conduction within the deposited material and heat losses due to convection and radiation. It also accounted for the heat input from the energy source using a Gaussian volumetric heat flux model.

To replicate the WAAM process realistically, the deposited track was divided into 64 clusters. Each cluster represented a segment of the deposited material and was activated sequentially to simulate the time-evolving nature of the deposition. The activation schedule was synchronized with the energy input, and the simulation time

step was selected to capture the rapid thermal changes occurring immediately after deposition. The material properties used in the model, including thermal conductivity, density, and specific heat capacity, were defined as temperature-dependent to capture the nonlinear response of 316L stainless steel under elevated temperatures. These parameters are pre-defined in ANSYS library.

The FEM framework allowed for full 3D simulation of both linear and semi-circular geometries. Simulations were run under varying energy source power levels to capture the influence of heat input on thermal profiles. The output of each simulation included spatially resolved temperature data collected via thousands of strategically placed probes. This data formed the basis for constructing and validating the functional surrogate model described in later chapters. The FEM simulation in ANSYS served as a controlled virtual experiment platform, enabling systematic investigation of thermal phenomena in WAAM and supporting the development of efficient, accurate predictive tools for thermal history modeling.

3.2 Governing Equations for Heat Transfer

The thermal behavior of WAAM processes is governed by transient heat transfer phenomena occurring within the deposited material and between the material and its surrounding environment. Capturing this behavior requires solving the governing PDEs that describe heat conduction in three dimensions, while simultaneously accounting for boundary heat losses due to convection and radiation. In this study, ANSYS solves the heat transfer equations using a finite element discretization over time and space, providing an accurate numerical representation of the thermal evolution during deposition.

3.2.1 Transient Heat Conduction Model

The principal equation governing the internal heat conduction in the deposited material is the transient heat conduction equation in three-dimensional Cartesian coordinates, expressed as:

$$\rho c \frac{\partial T}{\partial t} = \frac{\partial}{\partial x}\left(k_x \frac{\partial T}{\partial x}\right) + \frac{\partial}{\partial y}\left(k_y \frac{\partial T}{\partial y}\right) + \frac{\partial}{\partial z}\left(k_z \frac{\partial T}{\partial z}\right) + P(x, y, z, t). \tag{3.1}$$

where T is the transient temperature field [K], ρ is the density of the material [kg/m^3], and c is the specific heat capacity [J/kg·K]. The thermal conductivity coefficients k_x, k_y, and k_z [W/m·K] represent the directional conductivities in the x, y, and z directions, respectively. The term $P(x, y, z, t)$ is the volumetric heat generation rate [W/m^3] resulting from the applied heat source during deposition.

The heat conduction equation models the time-dependent diffusion of heat throughout the material body as influenced by internal energy sources. In the WAAM context, this includes the rapid heat input during wire melting as well as the redistribution of energy throughout the deposited region and into the base plate. The anisotropic form of the conductivity tensor allows the model to accommodate directional thermal transport, although in this study, isotropic thermal properties are assumed for simplification.

3.2.2 Radiation and Convection Losses

In addition to internal conduction, the model incorporates surface-based heat losses arising from both convection and thermal radiation to the surrounding environment. These effects are critical in WAAM processes, particularly for elevated surfaces exposed to ambient air during and after deposition.

The total heat loss per unit area from a surface is modeled through the combined convective and radiative heat transfer coefficient h, defined as:

$$h = \frac{\varepsilon_e \sigma_b (T^4 - T_a^4)}{T - T_a} + h_c, \tag{3.2}$$

where ε_e is the emissivity of the material surface (assumed to be 0.9 for stainless steel), σ_b is the Stefan-Boltzmann constant (5.67×10^{-8} W/m^2·K^4), T is the local surface temperature [K], and T_a is the ambient temperature [K], which is taken as 298.15 K (25°C) in this study. The term h_c is the convective heat transfer coefficient [W/m^2·K], empirically set to 10^{-5} W/mm^2·°C in accordance with previous studies on similar processes.

The combination of these heat loss mechanisms introduces natural cooling paths into the simulation and is essential for accurately modeling post-deposition temperature decay. Convective cooling dominates for elevated sections of the part exposed to air, while radiative losses become more significant at higher temperatures. These boundary conditions were applied uniformly across the exposed surfaces of the part and base plate during the simulation. Together, the conduction, convection, and radiation models ensure that the FEM simulation accurately reflects the real thermal conditions encountered in WAAM, supporting the generation of realistic training data for surrogate modeling.

3.3 Heat Source Modeling

Accurate representation of the heat source is a critical component of any thermal simulation in AM. In the context of WAAM, the heat input originates from an electric arc used to melt the metallic wire feedstock. The spatial and temporal distribution of this heat plays a central role in determining the resulting temperature field within

the deposited material and base plate. In this study, the heat input is modeled using a power-based volumetric heat source with a Gaussian spatial distribution, applied dynamically across discrete clusters that represent segments of the deposited track.

3.3.1 Gaussian Volumetric Source

The volumetric heat source in the simulation is governed by a Gaussian distribution centered on the location of active deposition. This approach allows for a realistic approximation of how energy from the arc is delivered into the material. The general expression for the heat flux density $q(x, y, z)$ is given by:

$$q(x, y, z) = \frac{3r_s P}{\pi r_0^2} \exp\left(-\frac{r^2}{r_0^2}\right), \tag{3.3}$$

where P is the total input power [W], r is the radial distance from the center of the heat source [mm], r_0 is the characteristic radius [mm] of the beam footprint, and r_s is a scaling factor defined by:

$$r_s = \frac{3R_0}{h}, \tag{3.4}$$

where R_0 represents the nominal radius and h the effective height of the heat source distribution. This spatial profile ensures that the majority of the energy is concentrated near the center of the active deposition zone, with exponentially decaying intensity toward the periphery.

The input power P is calculated from the electrical parameters of the process using:

$$P = V \cdot I \cdot \eta, \tag{3.5}$$

where V is the voltage [V], I is the current [A], and η is the efficiency of the heat transfer process, assumed to be 0.85 in this simulation, which is consistent with experimentally

reported arc efficiencies for GMAW-based WAAM processes (Goldak et al. 1984). The resulting power is then mapped to the finite element mesh using the `HGEN` command in ANSYS to apply heat generation rates over time to the active material elements.

3.3.2 Cluster Activation Method

During welding, material is melted through repeated cycles of low and high voltage. This process results in the depostion of discrete clusters of melted material. To realistically mimic the layer-by-layer and track-by-track deposition nature of WAAM, the simulated geometry is segmented into discrete clusters along the deposition path. Each cluster represents a volume of material corresponding to a small segment of the track, and is activated sequentially based on the deposition plan, i.e., torch travel speed and the duration of the voltage cycle.

In this study, each track, whether linear or semi-circular, is divided into 64 clusters of equal length. This is based on the assumption that the voltage cycle lasts 0.1 seconds. The temporal activation of these clusters simulates the progressive deposition of molten material, with each cluster being exposed to heat over a fixed time interval. The activation schedule ensures that heat is introduced only to regions where deposition is physically occurring, thereby preventing artificial preheating or unrealistic boundary conditions.

The cluster-based activation approach is implemented in ANSYS using element birth and death techniques, coordinated with time step controls to match the travel speed of the energy source. Each cluster corresponds to a deposition time increment of 0.1 seconds, collectively representing a full deposition time of 6.4 seconds for the entire track and 243.6 seconds for cooling down process, resulting in total 250 seconds for the whole process. This dynamic heat source application, combined with the Gaussian flux distribution and cluster activation, provides a robust thermal input model that

reflects the actual deposition conditions in WAAM, making it well-suited for producing high-fidelity data used in surrogate model development.

3.4 Geometry and Process Parameters

In this study, geometric modeling was performed programmatically using the CadQuery library in Python, which allowed for precise and automated generation of parametric STEP (.stp) files compatible with ANSYS.

3.4.1 Creating Geometries

Two distinct geometries were constructed to represent the fundamental deposition paths commonly encountered in WAAM: a straight linear track and a semi-circular arc. Both were designed to have a deposition length of 80 mm, ensuring equivalent material volume and process duration. The cross-section of the deposited material was fixed at 4.5 mm in width and 2.65 mm in height. The base plate, modeled as structural steel chosen among the materials in ANSYS library, had dimensions of 160 mm (length), 60 mm (width), and 10 mm (height).

The linear geometry was generated by extruding a rectangular cross-section along a straight 80 mm path centered on the base plate. In contrast, the semi-circular geometry was created by defining an arc with a radius of 25.515 mm, resulting in the same arc length as the linear case. The same cross-section was swept along this arc to form a semi-cylindrical track that adhered to the substrate. These two geometries were selected to serve as controlled test cases for evaluating the thermal behavior under different curvature conditions: the linear track provides a baseline scenario with minimal geometric complexity, while the curved path introduces curvature-driven effects in heat dissipation.

All geometric entities were constructed using the CadQuery Python library and exported as STEP files. These files were then imported into ANSYS SpaceClaim for pre-processing, including surface verification and preparation for meshing. All geometry was aligned with the global coordinate system to ensure consistent meshing, cluster activation, and probe placement.

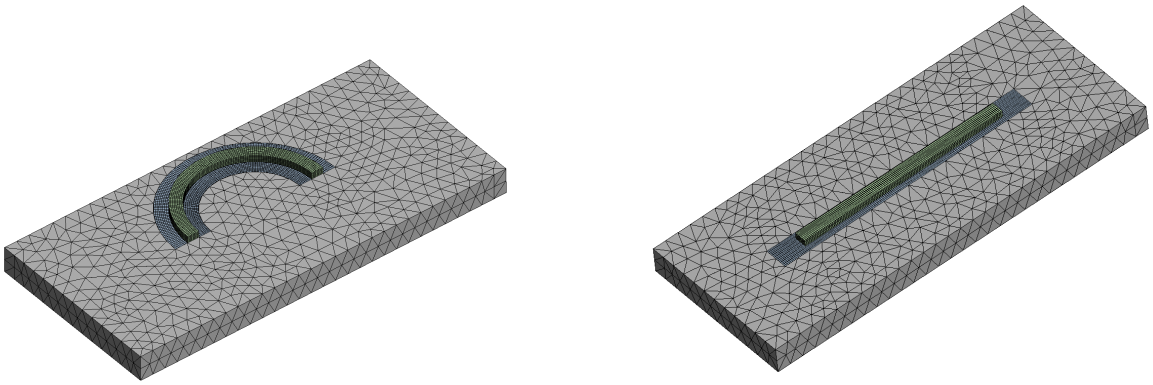

(a) (b)

Figure 3.1: Semi-circular (a) and linear (b) geometries in ANSYS environment

3.4.2 Meshing and Cluster Design

To ensure accurate thermal resolution, both geometries were discretized using a structured hexahedral mesh with a target element size of approximately 0.625 mm as shown in Fig. 3.1. A Cartesian mesh was used for the linear geometry, while a sweep mesh was applied to the semi-circular geometry. This mesh resolution provided a good balance between computational efficiency and accuracy, enabling the model to capture temperature gradients effectively without excessive simulation time.

The deposited track was divided into 64 clusters, each representing a deposition segment of 1.25 mm in length. These clusters formed the basis for sequential activation during the thermal simulation. In ANSYS, the clusters were defined using the mesh

element grouping feature, which enabled selective activation of elements via the element birth and death technique. The activation schedule was programmed such that each cluster received heat input for a duration of 0.1 seconds, mimicking the movement of the arc-based heat source across the track as shown in 3.2.

The resulting meshes are shown in Figure 3.1. Mesh quality was validated through skewness and aspect ratio checks, and regions of high thermal gradient, particularly near the track, substrate interface, were assigned denser mesh controls to improve accuracy. The resulting mesh structure supported the accurate capture of temperature transients and facilitated the high-resolution probe data collection needed for surrogate model training.

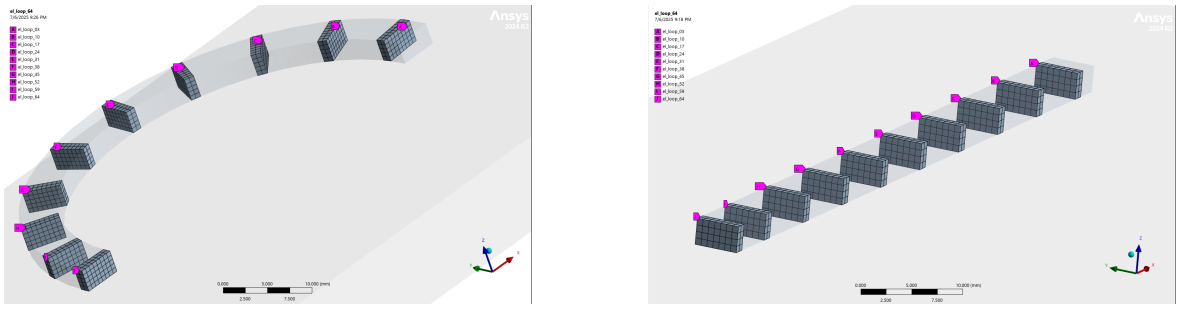

(a) (b)

Figure 3.2: Semi-circular (a) and linear (b) clustering in ANSYS environment

3.4.3 Deposition Parameters

The deposition parameters used in the simulation were based on typical WAAM process conditions for 316L stainless steel. The energy input was varied across six simulations using different power levels: 1396.67 W, 1440 W, 1483.33 W, 1505 W, 1526.67 W, and 1570 W. For all cases, the travel speed of the torch was maintained at 12.5 mm/s, resulting in a total deposition time of 6.4 seconds. An ambient temperature of 25°C

was also applied. The deposition rate was fixed at 149.0625 mm^3/s, and material properties such as density, specific heat capacity, and thermal conductivity were defined as temperature-dependent within ANSYS. These parameters provided a realistic physical basis for the simulation and allowed the thermal behavior to reflect conditions typically observed in WAAM fabrication.

Chapter 4

Methodology: Spatially Varying Functional Regression and Neural Network Models

4.1 Functional Model Framework

An earlier version of this work has been published in the proceedings of the 2025 IEEE Conference in Automation Science & Engineering (CASE) Dashti and Ruiz (2025). In this section, we develop a varying-coefficient functional model to predict the temperature history in single-layer, single-track wire-based MAM. We first represent the thermal history as a function of power, time-after-deposition, and location along the deposition path. Differences in thermal histories at distinct locations are then captured through coefficients that vary in space, modeled using a Gaussian process.

4.1.1 Temperature History Representation

Let $T(t, s)$ denote the temperature at spatial location s and simulation time t. Since the deposition process occurs in clusters, each cluster is deposited at a different time, shifting the start of the thermal history as shown in Figure 4.1. To construct a single model, we align the profiles using time after deposition τ. This alignment ensures that all profiles begin at $\tau = 0$, capturing the thermal peak and subsequent cooling consistently across locations. Thus, the thermal profile is modeled as $T(\tau, s)$. This

alignment ensures all thermal curves begin at the moment of deposition, enabling coherent modeling across spatial locations.

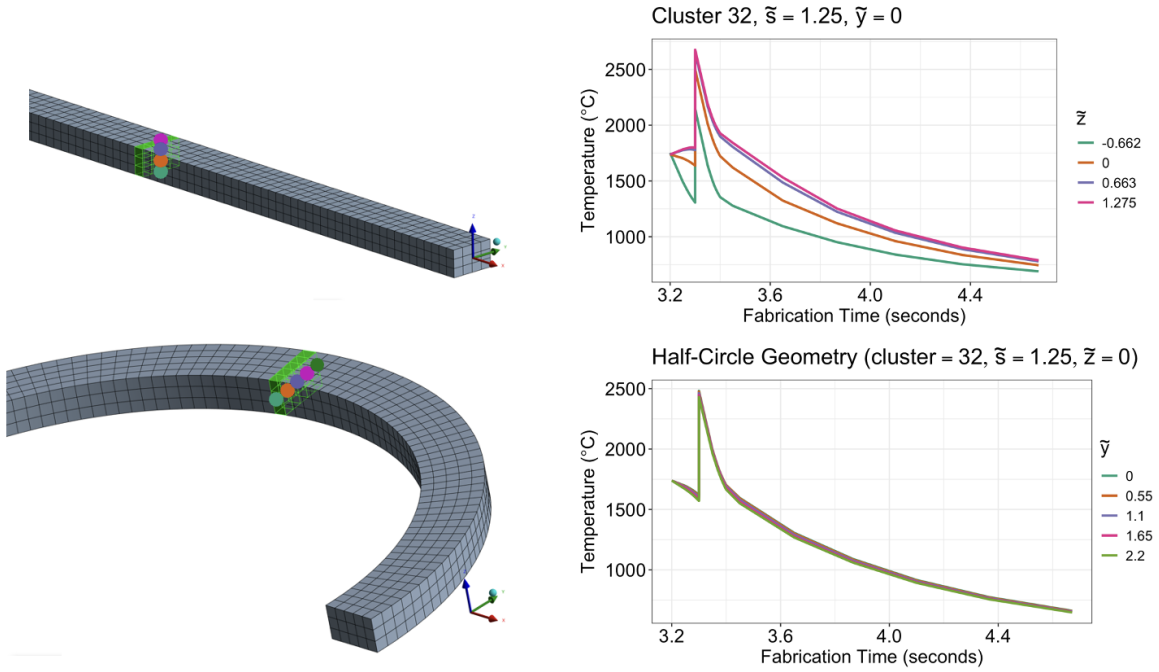

Figure 4.1: Comparison of thermal history at different locations in both geometries

During fabrication, the deposition a cluster of material induces sudden heating of the material near the end of the previous cluster while the material at the start of the cluster can have gradual heating. This effect is illustrated in Figure 4.1 where the top figures show the sudden increment after 0.1 seconds of deposition due to the deposition of the next cluster on the other hand, the bottom plots are for locations at the beginning of each cluster and show a slow heating pattern.

To model the heterogeneity in the behavior within each cluster, the location s is represented by cluster c that contains it and its location within the cluster $\tilde{s}$. That is, $c(s) = \lfloor s/\Delta \rfloor$ and $\tilde{s} = s - c(s) * \Delta$ where Δ is the length of material being deposited in each cluster.

4.1.2 Tensor Product of Functional Model

From the governing equations, it is clear that the initial temperature and temperature decay will be a function power P that introduced energy to the system to melt the material. Without loss of generality, P was scaled to be between 0 and 1 to represent the minimum and maximum levels that melt the material, respectively. Since energy and material might not be distributed uniformly during deposition, we also model the differences in the cross-sectional area of the weld. The modified locations $(\tilde{y}, \tilde{z})$ are the left-to-right and height coordinates with respect to the center of the track. As illustrated in Figure 4.1, temperature history shows rapid cooling immediately after deposition and the decreasing cooling rate soon after. By transforming temperature to the log-scale, the modeling of such temporal pattern is simplified as illustrated in Figure 4.2. Therefore, we consider a functional model for the log-temperature:

$$Y(\tau, P, \tilde{s}, c, \tilde{y}, \tilde{z}) = \log(T(\tau, P, \tilde{s}, c, \tilde{y}, \tilde{z})) = f(\tau, P, \tilde{s}, c, \tilde{y}, \tilde{z}) + \epsilon, \tag{4.1}$$

where $Y(\tau, P, \tilde{s}, c, \tilde{y}, \tilde{z})$ denotes the observed log–temperature and $T(\tau, P, \tilde{s}, c, \tilde{y}, \tilde{z})$ is the corresponding temperature. τ is time after deposition, P is the input power, $\tilde{s}$ is the scaled length coordinate along the deposition path and each cluster, c indexes the cluster, and $(\tilde{y}, \tilde{z})$ are the scaled cross-section probe location. The function $f(\tau, P, \tilde{s}, c, \tilde{y}, \tilde{z})$ is an unknown smooth function capturing the systematic structure of the temperature decay, and $\epsilon \sim \mathcal{N}(0, \sigma^2)$ is independent Gaussian noise with variance σ^2.

In our exploratory analysis, not included here due to space restrictions, the interactions between energy input and location are minimal when compared to the interactions between locations, therefore, the effect of P is modeled as additive in the log-scale. Therefore, the function f is modeled as two tensor-product basis of the effects of the

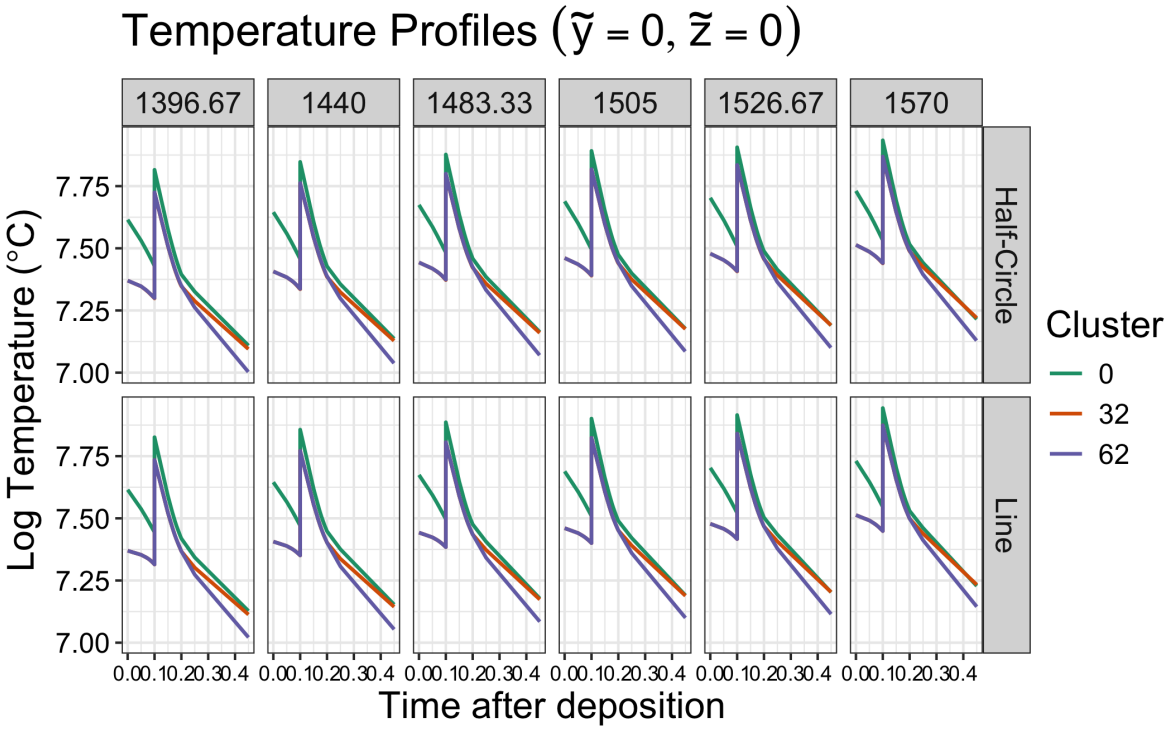

Figure 4.2: Temperature profiles for probes at different power levels and locations on both geometries at $\tilde{s} = 1.25$. The temperature after deposition was converted to the log scale.

time, location within cluster, and energy input with coefficients that vary along the cross-section location in each cluster:

$$\begin{aligned} f &= f^{(1)}(\tau, \tilde{s}, \tilde{y}, \tilde{z}, c) + f^{(2)}(\tau, P) \\ f^{(1)} &= \sum_{j=1}^{J} \phi_j^{(1)}(\tau, \tilde{s}) \beta_j^{(1)}(\tilde{y}, \tilde{z}, c) \\ f^{(2)} &= \sum_{j=1}^{J} \phi_j^{(2)}(\tau, P) \beta_j^{(2)}, \end{aligned} \tag{4.2}$$

where ϕ is a set of tensor product basis constructed as univariate basis of each covariate (Wood 2017). This representation allows the interpretability of the basis functions. The basis $\psi^{(2)}$ are constructed such that $f^{(2)}(\tau, 0) = 0$ and the changes on $f^{(2)}$ can

be interpreted as the effect of increasing the energy input. The effects of non-uniform changes in the thermal history across the cross-section and between clusters are modeled through the changes in β.

4.1.3 Spatially Varying Coefficients

The spatially varying coefficients $\beta_j^{(1)}(\tilde{y}, \tilde{z}, c)$ are modeled as an independent Gaussian Processes (GP) over cross-section and cluster index:

$$\beta_j^{(1)}(\tilde{y}, \tilde{z}, c) \sim \mathcal{GP}(0, \sigma_j^2 \kappa_j). \tag{4.3}$$

where κ_j is the correlation kernel function.

To reduce computation, we approximate the GP as a mixed effects problem with

$$\beta_j^{(1)}(\tilde{y}, \tilde{z}, c) \approx \alpha_{j,0} + \sum_{\ell=1}^{m} \psi_\ell(\tilde{y}, \tilde{z}, c) \cdot \alpha_{j,\ell}, \tag{4.4}$$

where ψ is a set of GP basis constructed by selecting m support locations and setting $\Psi = \mathrm{K}_1 \mathrm{K}_2^{-1/2}$ with K_2 being the correlation matrix between support locations and K_1 the correlation matrix between locations in the data set and support locations Kammann and Wand (2003). $\alpha_{j,0}$ is the intercept coefficient, that is, it represent the fixed effect coefficient for the model. $\alpha_{j,\ell}$ being the corresponding random coefficients for the GP basis. The random parameters follow the Multivariate Gaussian distribution with mean zero and standard deviation σ_j.

These Gaussian prior for $\alpha_{j,\ell}$ are equivalent to an Ridge penalty in the corresponding penalized likelihood. Equivalently, estimation of the spatially varying coefficients can be viewed as solving a ridge-regularized least-squares problem, where large deviations of the coefficients at the support locations are discouraged according to the covariance

K_j. This ridge-type regularization stabilizes the fit of the spatially varying functional component, particularly in regions with sparse observations or collinearity among basis functions.

To construct ψ, the correlation matrix is assumed to be common between GPs and be composed by a separable stationary kernel function κ such that:

$$\kappa = \kappa_y(\theta_y|\tilde{y} - \tilde{y}'|)\kappa_z(\theta_z|\tilde{z} - \tilde{z}'|)\kappa_c(|c - c'|, \theta_c). \tag{4.5}$$

The well known Matern kernel is considered for modeling κ_y and κ_z with θ representing the inverse-range parameter. κ_c is modeled using the Wendland function (Wendland 1998) is considered to implement sparse correlations between clusters with θ_c representing the maximum distance between points for which correlation is positive.

4.1.4 Implementation and Training

The functional was implemented in the *R* software. The model is trained in three steps: 1) find an initial guess of $\boldsymbol{\beta}^{(1)}(\tilde{y}, \tilde{z}, c)$ and $\boldsymbol{\beta}^{(2)}$, 2) estimate θ and σ_j for all locations based on the initial guess of $\boldsymbol{\beta}^{(1)}(\tilde{y}, \tilde{z}, c)$, and 3) obtain a final estimate of $\boldsymbol{\alpha}$ and $\boldsymbol{\beta}^{(2)}$.

To compute the initial estimate of the $\boldsymbol{\beta}^{(1)}(\tilde{y}, \tilde{z}, c)$ and $\boldsymbol{\beta}^{(2)}$, the following linear regression problem is solved

$$\boldsymbol{y} = \tilde{\Phi}^{(1)}\tilde{\boldsymbol{\beta}}^{(1)} + \Phi^{(2)}\boldsymbol{\beta}^{(2)} + \epsilon \tag{4.6}$$

where $\boldsymbol{y}$ is the vector of all observations sorted by unique locations $(\tilde{y}, \tilde{z}, c)$, $\tilde{\Phi}^{(1)}$ is a block diagonal matrix with blocks being the the basis corresponding to each unique location, $\tilde{\boldsymbol{\beta}}$ is the vector of concatenated coefficients for each unique location.

After applying standard least-squares, initial values for $\hat{\boldsymbol{\beta}}_j^{(1)}$ are obtained for all unique locations. Then, the log-likelihood function for the GP is maximized as

$$\max_{\theta,\sigma_j} \; -\frac{1}{2}\sum_{j=1}^{J}\sigma_j^{-2}\hat{\boldsymbol{\beta}}_j^{T(1)}\mathrm{K}^{-1}\hat{\boldsymbol{\beta}}_j^{(1)} - \frac{1}{2}\ln|\mathrm{K}|\sum_{j=1}^{J}\ln(\sigma_j^2) \tag{4.7}$$

where K is the covariance matrix between unique locations in the training set.

From solving Eq. 4.1.4, we obtain the $\hat{\theta}$ and $\hat{\sigma}_j$ for $j = 1, \ldots J$ to construct ψ. The full model can be expressed as a mixed effects of the form

$$\boldsymbol{y} = \Phi^{(1)}\boldsymbol{\alpha}_0 + \Phi^{(2)}\boldsymbol{\beta}^{(2)} + \mathrm{Z}\tilde{\boldsymbol{\alpha}} + \epsilon \tag{4.8}$$

where $\Phi^{(1)}\boldsymbol{\alpha}_0$ corresponds to the main effect regardless of location, $\tilde{\boldsymbol{\alpha}} = \{\boldsymbol{\alpha}_1, \ldots \boldsymbol{\alpha}_J\}$ is a vector of concatenated coefficients for each basis in $\Phi^{(1)}$. $\mathrm{Z} = [\Phi_{(1,1)}^{(1)}\Psi, \Phi_{(2,1)}^{(1)}\Psi, \ldots, \Phi_{(J,n)}^{(1)}\Psi]$ is a matrix of random effects constructed by multiplying the column vectors $\Phi_{(j,i)}^{(1)}$ corresponding to basis j and unique location $i = 1, \ldots, n$. To maintain dimensionality criteria, $\Phi_{(j,i)}^{(1)}$ is constructed by adding zeros to locations that do not correspond to the ith unique location. This mixed effects problem is solved using the Laplace approximation with fixed values of θ and σ, and σ_j obtained from the previous steps.

4.2 Neural Network Framework

This section describes the neural-network (NN) framework developed as a fast surrogate model for predicting the thermal history in WAAM. The NN is trained and evaluated on the same simulation-derived dataset that was previously used to fit the functional model, ensuring a direct and fair comparison between the two approaches. For each

observation, the input features of the neural network are the same as in the functional model. For notation convenience, we define:

$$x = (\tau, P, \tilde{s}, c, \tilde{y}, \tilde{z}).$$

The remainder of this sections focuses on the NN's architecture, hyperparameter optimization, and training procedure.

4.2.1 Network Architecture

The NN model is a deep fully connected network designed to capture the nonlinear spatiotemporal dependence of the temperature field on the process variables as shown in Figure 4.3. The architecture begins with an input layer of six neurons, corresponding to the six input features. This is followed by a stack of L fully connected hidden layers. Each hidden layer applies a linear transformation, followed by batch normalization, a tanh activation, and dropout with probability p_{drop}, in that order.

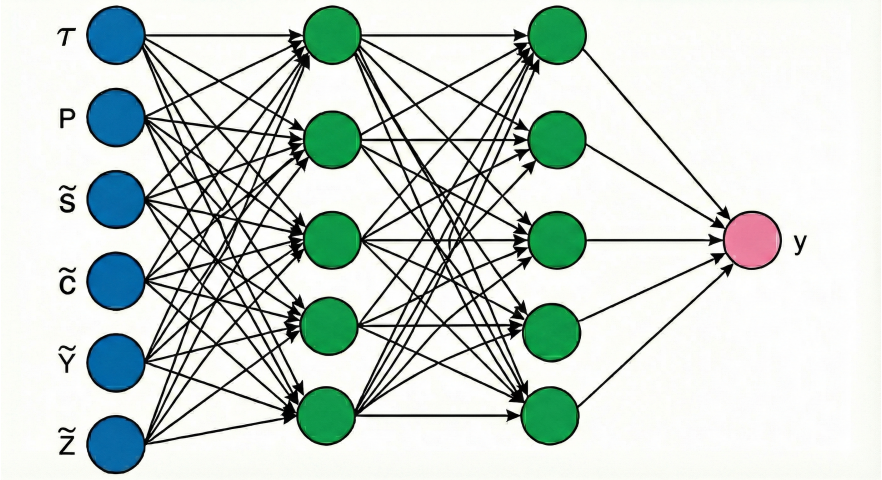

Figure 4.3: The architecture of Neural Network

The final hidden representation is passed to an output layer consisting of a fully connected linear transformation mapping to a scalar. A Softplus activation is then applied to this scalar output to ensure positivity of the predicted temperature in the log scale. In compact form, for an input $x \in \mathbb{R}^6$ the network computes

$$\begin{aligned} h^{(\ell)} &= \mathrm{Dropout}\big(\tanh\big(\mathrm{BN}\big(W^{(\ell)}h^{(\ell-1)} + b^{(\ell)}\big)\big)\big)\,, \quad \ell = 1, \ldots, L, \\ \hat{y} &= \mathrm{Softplus}\big(W^{(L+1)}h^{(L)} + b^{(L+1)}\big)\,. \end{aligned} \tag{4.9}$$

The depth L, hidden-layer width, and dropout probability are all selected automatically through Bayesian hyperparameter optimization.

4.2.2 Hyperparameter Optimization

The model was developed using PyTorch v2.1. Hyperparameter selection is performed using the Optuna (Akiba et al. 2019) framework with the Tree-Structured Parzen Estimator (TPE) (Watanabe 2023) sampler. TPE consists of splitting the search region into promising and non-promising sub-regions and selecting the next network configuration based on the probability of improvement from the promising and non-promising posterior distributions (Watanabe 2023).

For each geometry, a separate Optuna study is created, and the key architectural and training hyperparameters of the NN are tuned jointly within this framework. The search space includes the number of hidden layers L, varied over the discrete set $6, \ldots, 12$, and the hidden-layer width H, chosen from $16, 32, 64$. The learning rate η is sampled on a logarithmic scale within the continuous range $[10^{-4}, 10^{-2}]$. The batch size B is selected from $16, 32, 64$, and the dropout probability p_{drop} is drawn from the continuous interval $[0.0, 0.5]$. Each trial in the Bayesian optimization corresponds to one configuration of $(L, H, \eta, B, p_{\mathrm{drop}})$.

During Bayesian optimization, grouped 3-fold cross-validation is used as the target metric for minimization. The cluster variable is used as identifier to define the groups. In this setup, entire clusters are assigned either to the training or the validation set within each fold, so that no cluster appears in both. This mimics the intended use of the model, where predictions are required for clusters that were not directly used for training. The objective value reported to Optuna is the average validation MSE across the three folds. After 10 Bayesian trials, the configuration with the lowest cross-validated MSE is selected as the best hyperparameter setting for that geometry. Once the optimal hyperparameters are identified by Optuna, a final model is trained on the *entire* training set for each geometry using the selected configuration. This model is then evaluated on two test sets as in functional model.

4.2.3 Training Procedure and Early Stopping

Given the large size of the dataset (on the order of 10^6 samples per geometry), all computations are performed in mini-batches to be processed within GPU memory. The features and target are converted to single-precision tensors and wrapped in a custom `Dataset` and `DataLoader` implementation. All neural network models were trained on an NVIDIA RTX 5000 Ada Generation Laptop GPU using the Adam optimizer and mean squared error as the loss function. Let $D_{\text{train}} = \{(x_i, y_i)\}_{i=1}^{N_{\text{train}}}$ denote the training set and D_{val} the validation subset associated with a given cross-validation fold. For any dataset D, the MSE loss is written as:

$$\mathcal{L}_{\text{MSE}}(\theta; D) = \frac{1}{|D|} \sum_{(x,y)\in D} \big(f_\theta(x) - y\big)^2,$$

where f_θ denotes the neural network with parameters θ. During training, mini-batches drawn from D_{train} are used to update θ, while the validation loss $\mathcal{L}_{\text{MSE}}(\theta; D_{\text{val}})$ is monitored to assess generalization within the fold.

Each model is trained for a maximum of fifty epochs. However, to prevent overfitting and unnecessary computation, an early-stopping mechanism is applied. Let $\ell_{\text{val}}^{(t)} = \mathcal{L}_{\text{MSE}}\left(\theta^{(t)}; D_{\text{val}}\right)$ denote the validation loss at epoch t. Training is terminated if the validation loss does not improve by at least $\delta = 10^{-5}$ for 15 consecutive epochs. When early stopping occurs, the parameter vector is reset to $\hat{\theta} = \arg\min_t \ell_{\text{val}}^{(t)}$, so that the final model corresponds to the epoch achieving the lowest validation loss.

During training, mini-batches were shuffled with the last batch being dropped to ensure that every batch has the same number of samples. This stabilizes batch normalization statistics and prevents the final, smaller batch from introducing distributional inconsistencies. In contrast, during validation and test evaluation, all samples were retained and no batches were dropped, since batch normalization layers operate in evaluation mode and no longer depend on batch-level statistics. Validation loss was recorded at the first epoch and subsequently every ten epochs, allowing consistent monitoring of training stability and convergence behavior throughout the optimization process.

Chapter 5

Results: Accuracy and Computational Cost

5.1 Integrated mean absolute relative error to meassure accuracy of functional predictions

To evaluate prediction accuracy at each probe we use the integrated mean absolute relative error (MARE) between the simulated temperature history $T(\tau)$ and the surrogate prediction $\hat{T}(\tau)$ over a given time window $[l, u]$. Following Lin et al. Lin et al. (2024), MARE is defined as

$$\text{MARE} \;=\; \frac{\displaystyle\int_l^u \left|T(\tau) - \hat{T}(\tau)\right| \,\mathrm{d}\tau}{\displaystyle\int_l^u |T(\tau)| \,\mathrm{d}\tau}. \tag{5.1}$$

This quantity is scale-invariant and can be interpreted as the ratio of the area of the error in temperature prediction and the area of the true temperature profile.

To better isolate different stages of the thermal history, we partition it into three phases based on time-after-deposition: a heating phase that lasts up to the first 0.2 s, a rapid cooling phase from 0.2 s to 2 s, and a long-term cooling phase afterwards. For each probe and phase, we compute the MARE in Eq. (5.1), and then average across probes at the same path location and cross-sectional height. The figures in this section

report these average MARE values for the functional model and the neural network surrogate.

5.2 Creating Probes for Data Collection

To analyze the spatiotemporal evolution of temperature during WAAM deposition, virtual temperature probes were embedded throughout the deposited track. These probes were used to extract high-resolution thermal history data directly from the FEM simulation. Probe placement was performed systematically to ensure representative sampling across both the deposition path and the weld cross-section as shown in Figure 5.1.

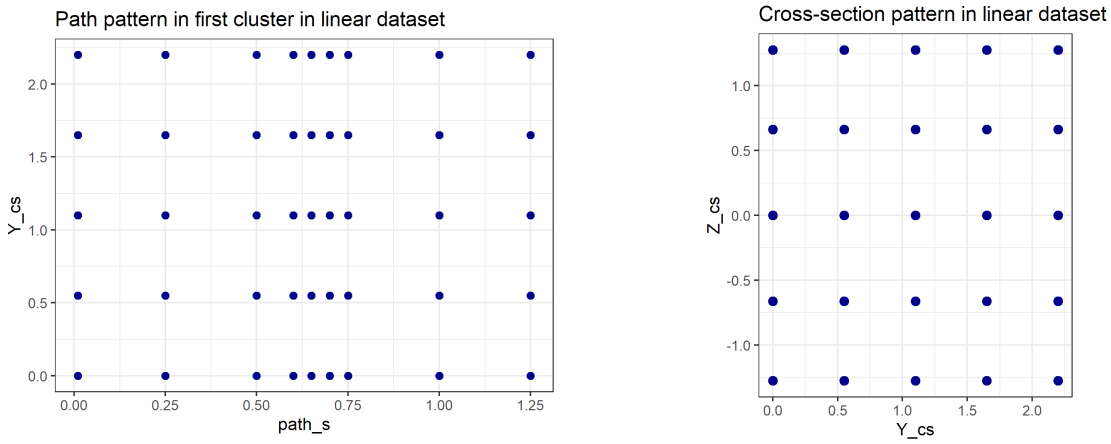

Figure 5.1: Probes placement along path and cross-section in linear geometry

The deposition track was divided into 64 clusters, all selected. This included all edge clusters and evenly spaced interior clusters to capture both boundary and mid-path thermal behavior. Within each selected cluster, probes were positioned at multiple longitudinal offsets relative to the cluster length, denoted as $\tilde{s} = \{0.01, 0.25, 0.50, 0.60, 0.65, 0.70, 0.75, 1.00, 1.25\}$ mm. At each of these positions, 25 probes were placed across the YZ cross-section to record thermal variation through the height and width of the

deposited material. Probes were created through a code which is compatible with ANSYS Parametric Design Language (APDL). The code is available at appendix B. In total, 14,440 probes ($64 \times 9 \times 25$) were used in the simulations for each power level, forming the basis for model training and evaluation in subsequent chapters.

5.3 Data Split into Training and Test sets

To evaluate the surrogate models under different scenarios, the simulation-derived dataset for each geometry was partitioned into three disjoint subsets: a training set, a between-cluster (BC) test set, and a within-power (WP) test set. The splitting strategy was designed to probe two main questions: (i) how well the models interpolate to spatial regions (clusters) that were not used for training at the same power levels, and (ii) how well they generalize to power levels that are not present in the training set.

Four representative power levels were selected within the overall process window, $\mathcal{P}_{\text{train}} = \{1396.67,\ 1483.33,\ 1526.67,\ 1570\}\,\text{W}$, and used as the basis for both the training and BC test sets. Along the 80 mm deposition path, the 64 clusters were indexed as cluster_int $= 0, \ldots, 63$. A subset of these clusters, $\mathcal{C}_{\text{train}} = \{0, 1, 2\} \cup \{3, 6, 9, \ldots, 60\} \cup \{61, 62, 63\}$, was assigned to the training set. This corresponds to using three consecutive clusters at each end of the path together with approximately every third cluster in the interior, providing coverage along the entire track while leaving non-adjacent clusters for testing. Thus, the *training set* for each geometry consists of all observations with $P \in \mathcal{P}_{\text{train}}$ and $c \in \mathcal{C}_{\text{train}}$. The *BC test set* contains all remaining clusters at the same four power levels, i.e., $P \in \mathcal{P}_{\text{train}}$ and $c \notin \mathcal{C}_{\text{train}}$, and is used to assess how well the models interpolate to spatial regions along the path that were never seen during training but share the same process conditions. Finally, the *within-power (WP) test set* comprises all observations at power levels outside $\mathcal{P}_{\text{train}}$ over

all clusters. These cases typically correspond to intermediate power levels within the experimental window and are used to evaluate generalization in the power dimension, i.e., interpolation or mild extrapolation to new energy inputs while preserving the same geometric configuration.

An additional restriction was imposed on the cross-sectional locations used for modeling. We did not include probe points at the bottom of the bead ($Z = -1.25$ mm in the transformed coordinate system), because this region is in direct contact with the base plate and exhibits different thermal behavior due to strong conduction into the substrate. In practice, the prediction of temperature near the top of the deposited track is of greater interest, since this is the region with the highest heat accumulation and the region that will interact with subsequent layers in multi-layer builds. Future work will consider partitioned-domain strategies in which different Gaussian process hyperparameters or basis structures are used for bead–substrate interfaces and for interior cross-sections, allowing the surrogate models to better accommodate such boundary effects.

5.4 Best Hyperparameters for NN Training

For the linear geometry, the Bayesian optimization procedure converged to a relatively deep architecture with a moderate hidden width and small dropout. The selected configuration consists of nine hidden layers with thirty-two units per layer, a learning rate on the order of 10^{-4}, a batch size of sixty-four, and a dropout probability of approximately 0.10. This setting reflects a compromise between expressiveness and regularization, allowing the network to capture the nonlinear thermal response while maintaining stable training.

For the circular geometry, the optimizer selected a slightly shallower architecture with the same hidden width but a somewhat larger dropout probability and a lower learning rate. In this case, the optimal configuration contains eight hidden layers with thirty-two units per layer, a learning rate again on the order of 10^{-4} but smaller than in the linear case, a batch size of sixty-four, and a dropout probability of approximately 0.13. The increased dropout and reduced learning rate are consistent with the additional geometric complexity of the circular track and help to regularize the model while ensuring smooth convergence.

Table 5.1 summarizes the final hyperparameter configurations for the linear and circular geometries, together with training times on the GPU.

Table 5.1: Summary of selected neural-network hyperparameters and training runtimes for the linear (L) and circular (C) geometries.

Quantity	Linear geometry (L)	Circular geometry (C)
Number of layers L	9	8
Hidden dimension H	32	32
Learning rate η	3.84×10^{-4}	1.75×10^{-4}
Batch size B	64	64
Dropout p_{drop}	0.0998	0.1294
Training time t_{train}	115 min	56 min

5.5 Varying Coefficients Patterns for the Functional Model

Figures 5.2a and 5.2b show the estimated coefficients associated with the interaction between the temporal intercept basis $\phi_1(\tau)$ and the spatial basis functions $\phi_k(s)$ for the

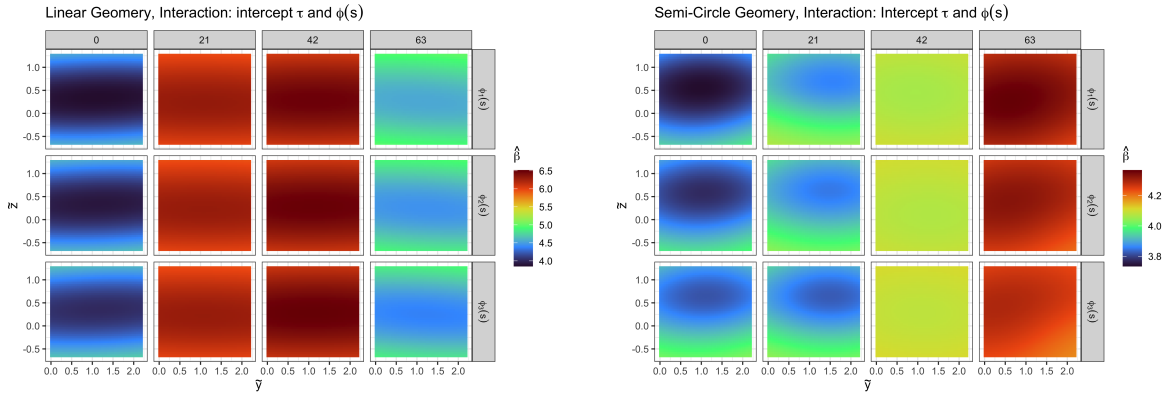

(a) Linear geometry

(b) Circular geometry

Figure 5.2: Comparison of spatially varying coefficient behavior for the interaction between the intercept and the spatial basis functions across both geometries.

linear and semi-circle geometries, respectively. For the linear geometry, the coefficient surfaces are consistently larger values of $\hat{\beta}_{1k}$ in the mid–upper part of the cross-section. The coefficients change significantly across clusters, suggesting that clusters at the edges of the part (i.e., 0 and 63) have a very different thermal history pattern that those at the interior. The first spatial basis affects the beginning of each cluster, while the second basis affects the middle and the last basis affects the end of the cluster. The patterns seem consistent across all sections of basis $\phi(s)$, that is, the overall effect of the temporal intercept is stable within clusters. In contrast, for the semi-circle geometry the intercept-spatial interaction exhibits consistent changes alongside the clusters. As the deposition proceed, the curved geometry promotes additional heat build-up and a more homogeneous baseline temperature field in later clusters. Nevertheless, the range of the coefficient is significantly lower than the range observed in the linear geometry. This behavior is explained by the interactions between coefficients of different basis.Figure 5.3 shows the coefficients for the interaction between the first B-spline temporal basis $\phi_2(\tau)$ and the leading spatial basis $\phi_1(s)$. For both geometries, the coefficients are inversely correlated to the coefficients of the interaction between

$\phi_1(\tau)$ and $\phi(s)$. This indicates that the clusters 21 and 22 have a somewhat simpler pattern for the linear geometry while in all other cases the temperature history pattern is more complex and cannot be captured as much by a constant temperature.

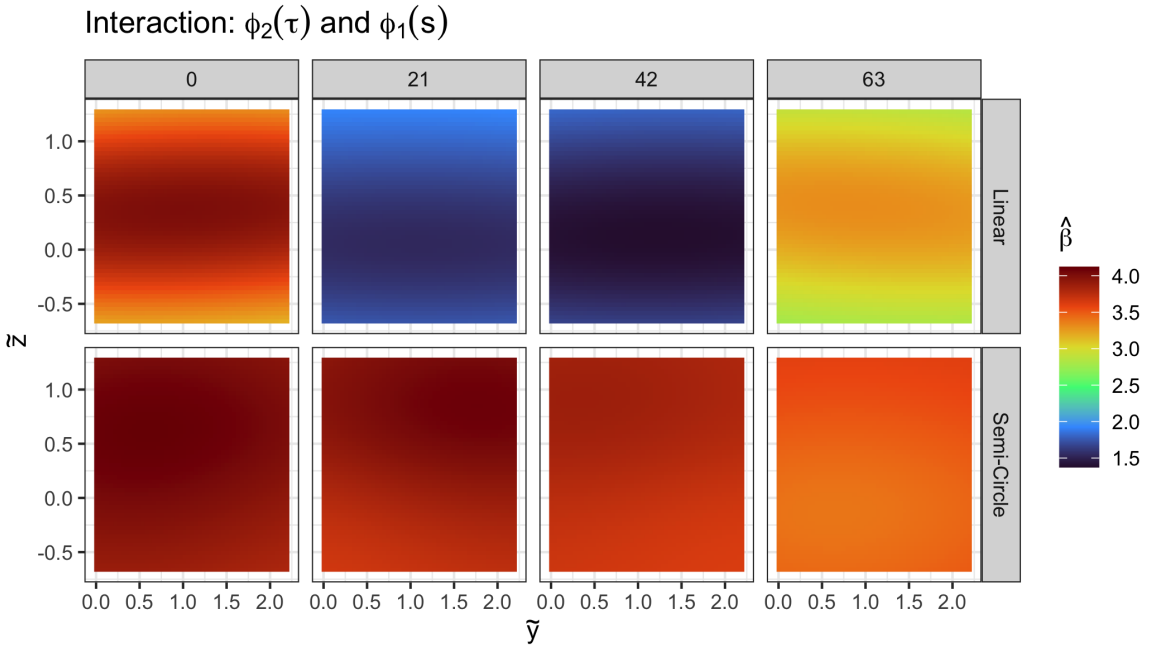

Figure 5.3: Estimated coefficients for the interaction between the first B-spline in time and the spatial basis across clusters for both geometries.

Figure 5.4 shows the estimated coefficients associated with the interaction between the spike basis at $\tau = 0.1$, denoted $\phi_{\text{spk}}(\tau)$, and the spatial basis functions $\phi_k(s)$. For both geometries, the basis at the end of the cluster $\phi_3(s)$ have a significant impact while the ones at the beginning are negligible. This is expected since the impact of the deposition of the next cluster is more pronounce on the end of the current cluster. Moreover, the interactions with $\phi_2(s)$ and especially $\phi_3(s)$ exhibit pronounced vertical gradients and a clear increase in magnitude toward the final clusters. This behavior reflects the fact that the early post-deposition thermal spike is stronger near the upper portion of the bead and intensifies as heat accumulates along the deposition path. Note that the parameter fields for the last cluster are not zero due to transfer of knowledge

between locations, however, the last cluster does not suffer this extreme heat transfer in the simulation.

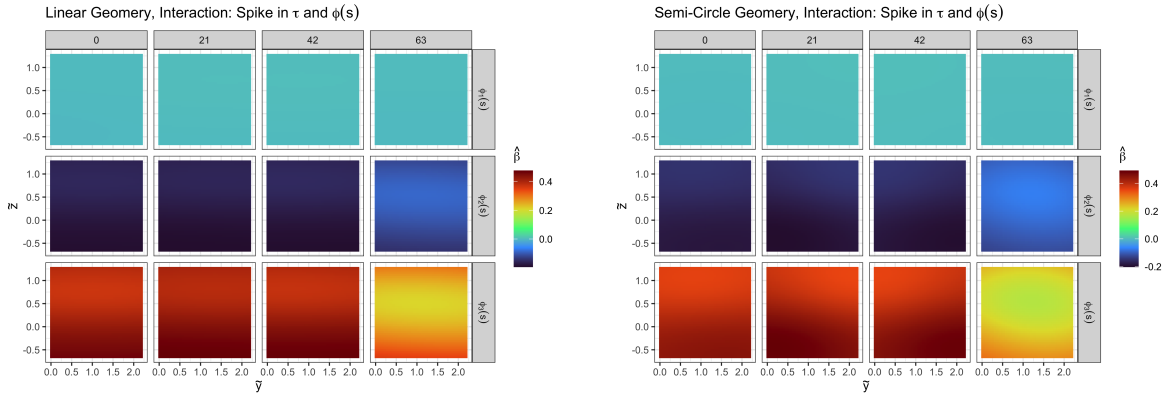

(a) Linear geometry

(b) Circular geometry

Figure 5.4: Comparison of spatially varying coefficient behavior for the interaction between the spike and the spatial basis functions across both geometries

5.6 Accuracy on circular geometry

Figure 5.5 shows the average MARE for the circular geometry on the training set. Most profiles remain below 0.1, indicating that both surrogates fit the simulation data well, although isolated spikes up to about 0.2 appear during the cooling phase, similar to what is observed in the WP test set. Figure 5.6 reports the BC results. Across all power levels, the average MARE is mostly below 0.1, with the smallest errors in the rapid cooling and cooling phases and the largest errors during heating, where sharp temperature peaks immediately after deposition are most difficult to approximate. Figure 5.7 summarizes the WP results, where intermediate power levels are not seen during training. In this case, the MARE increases near the beginning of the path—especially at the middle row and in the heating phase—but generally decreases along the path and during cooling. Overall, the circular-geometry results indicate that

both surrogates can interpolate across clusters and power levels, with noticeably better accuracy in the cooling-dominated portions of the histories.

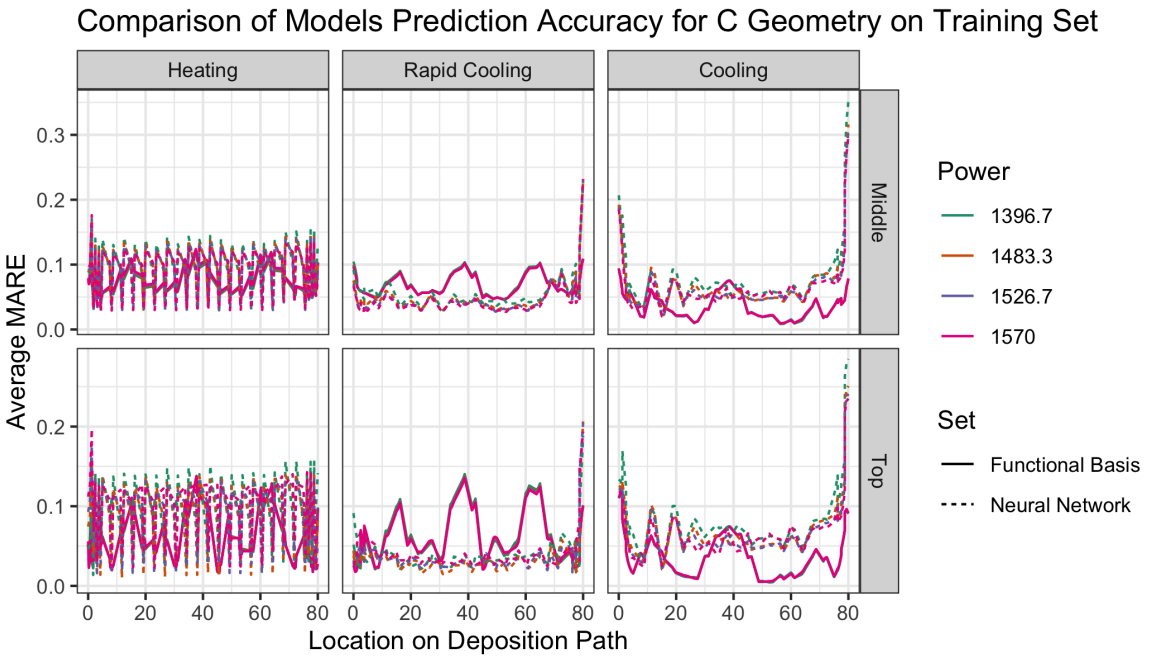

Figure 5.5: Average MARE across probes for the circular geometry, Train test set.

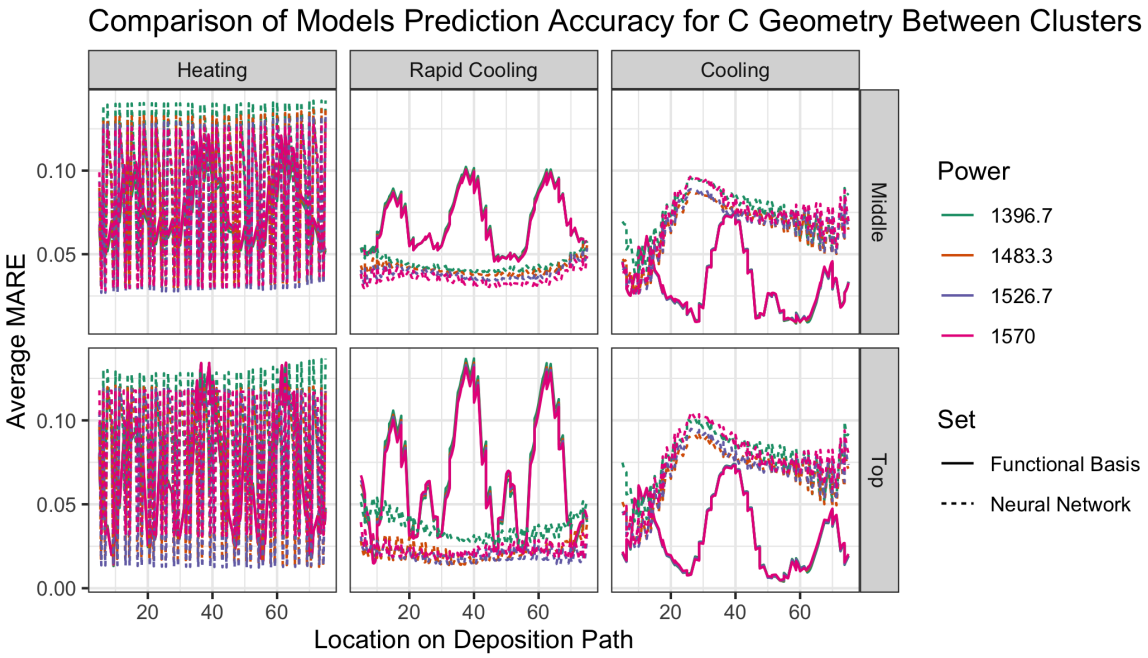

Figure 5.6: Average MARE across probes for the circular geometry, BC test set.

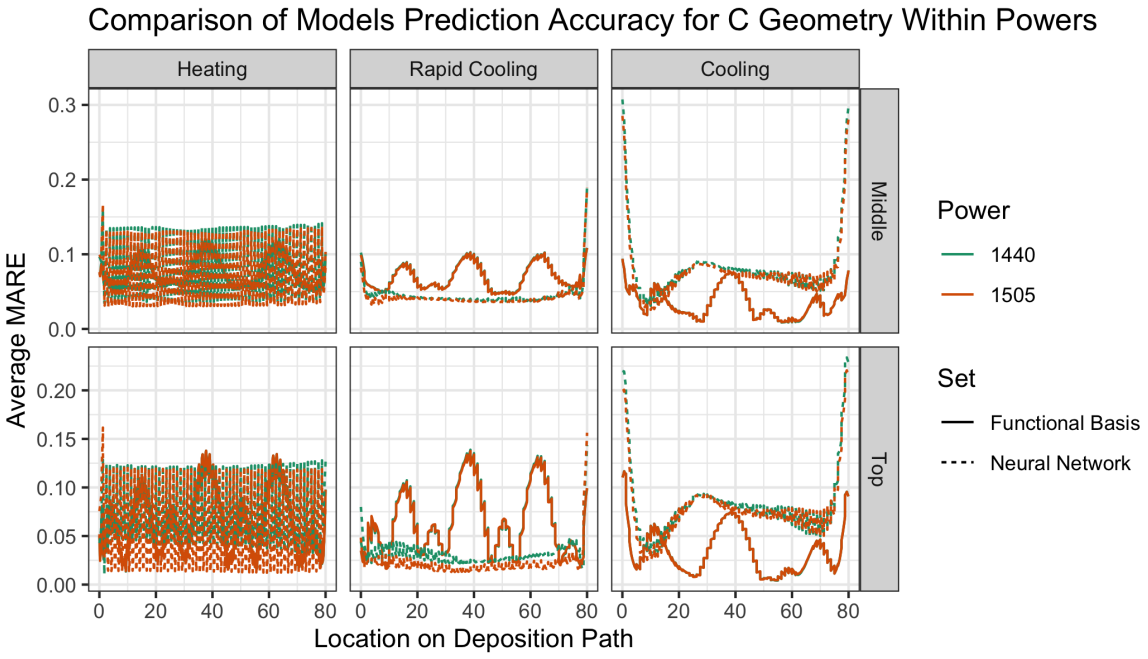

Figure 5.7: Average MARE across probes for the circular geometry, within-power test set.

5.7 Accuracy on linear geometry

The corresponding MARE profiles for the linear geometry are shown in Figure 5.8, 5.9 and 5.10. Compared with the circular case, the error patterns are more uniform along the deposition path, which is consistent with the absence of curvature-induced variations. However, this only applies to the functional basis model. The neural network result in linear geometry fluctuates more compared to circular geometry. For the BC split (Figure 5.9), most locations exhibit MARE between about 0.03 and 0.12, again with smaller errors in the rapid cooling and cooling phases. In the within-power split Figure 5.10, unseen power levels lead to higher variability near the start of the path during heating, but MARE gradually decreases downstream as the thermal field becomes smoother in time and space. Taken together, the linear-geometry results confirm that the surrogate framework generalizes across clusters and power levels when the deposition path is simpler.

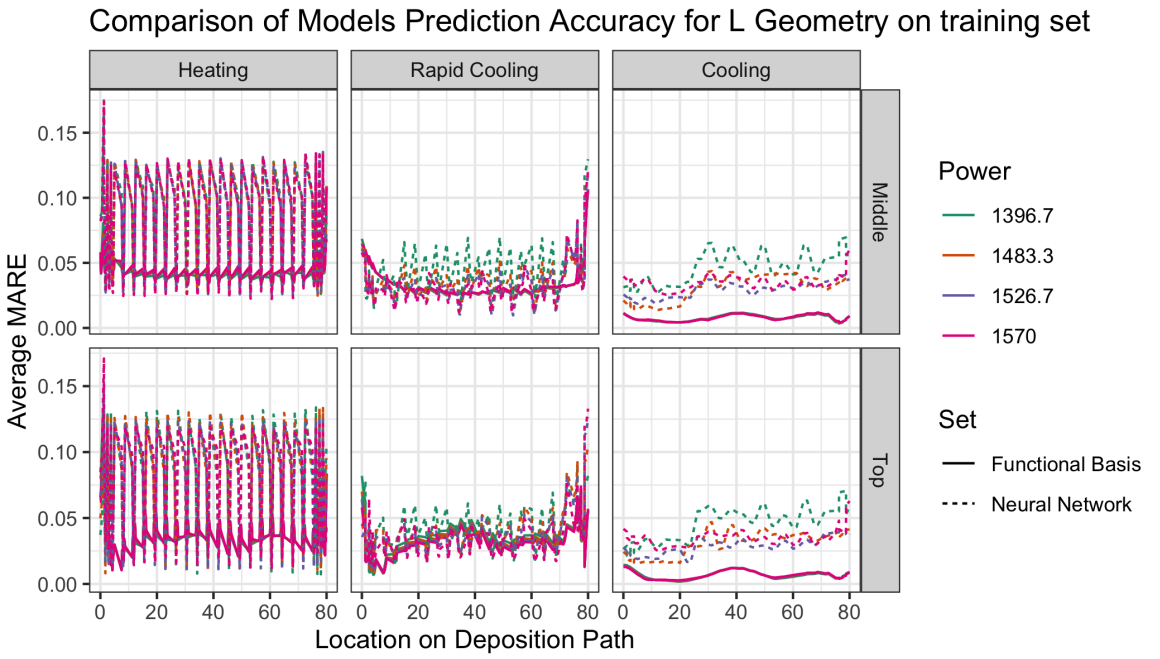

Figure 5.8: Average MARE across probes for the linear geometry, Train test set.

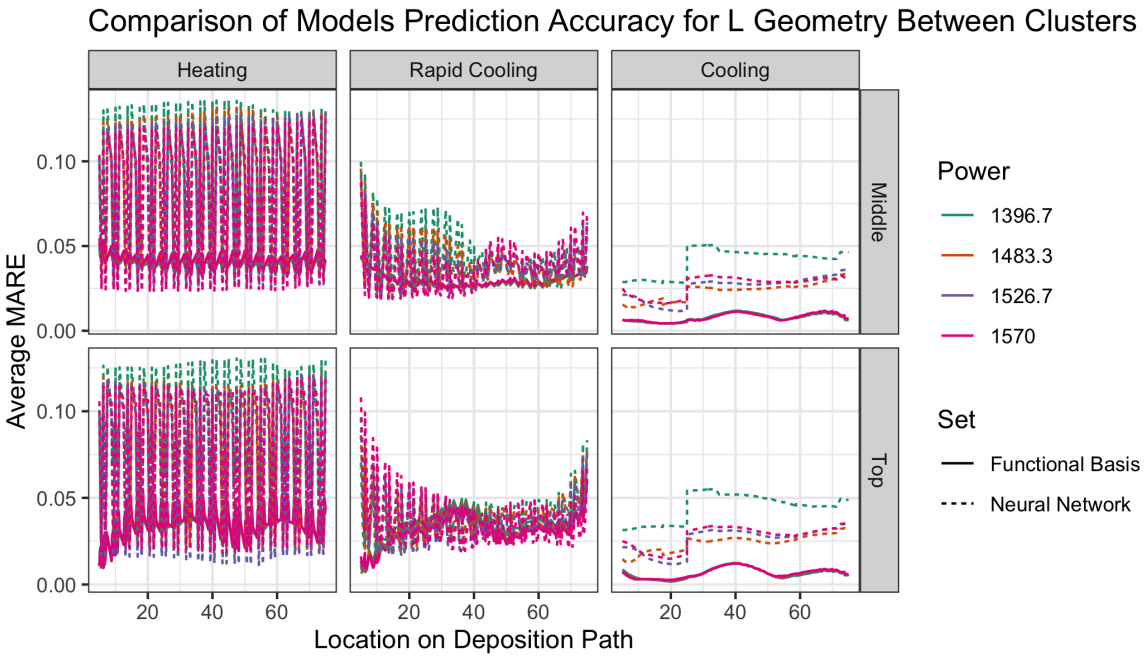

Figure 5.9: Average MARE across probes for the linear geometry, BC test set.

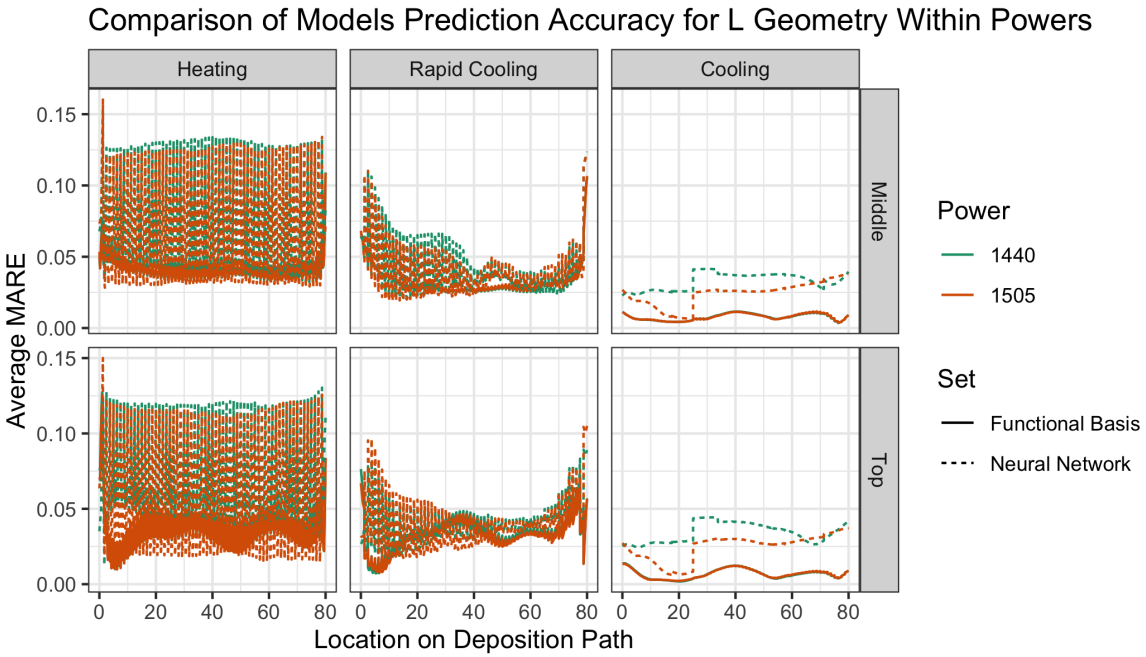

Figure 5.10: Average MARE across probes for the linear geometry, within-power test set.

Across both geometries, three consistent trends appear: (i) errors are largest in the heating window, where sharp local peaks and re-heating events are hardest to approximate; (ii) rapid cooling and long-term cooling phases are predicted more accurately; and (iii) interpolation across clusters is generally easier than interpolation across power levels, especially near the start of the path.

5.8 Pointwise comparison of temperature histories

Figures 5.11 and 5.12 provide pointwise comparisons at a representative middle probe for the circular and linear geometries. In both cases, the surrogates capture the overall shape of the temperature history, with the largest discrepancies confined to the very short heating phase where the FEM solutions exhibit sharp peaks. During rapid cooling, the predicted curves closely follow the simulated decay, and in the long-term cooling window the three curves are nearly indistinguishable. These examples are consistent with the MARE patterns: reproducing the detailed shape of the heating peak is most challenging, whereas the slower diffusive cooling behavior is well captured.

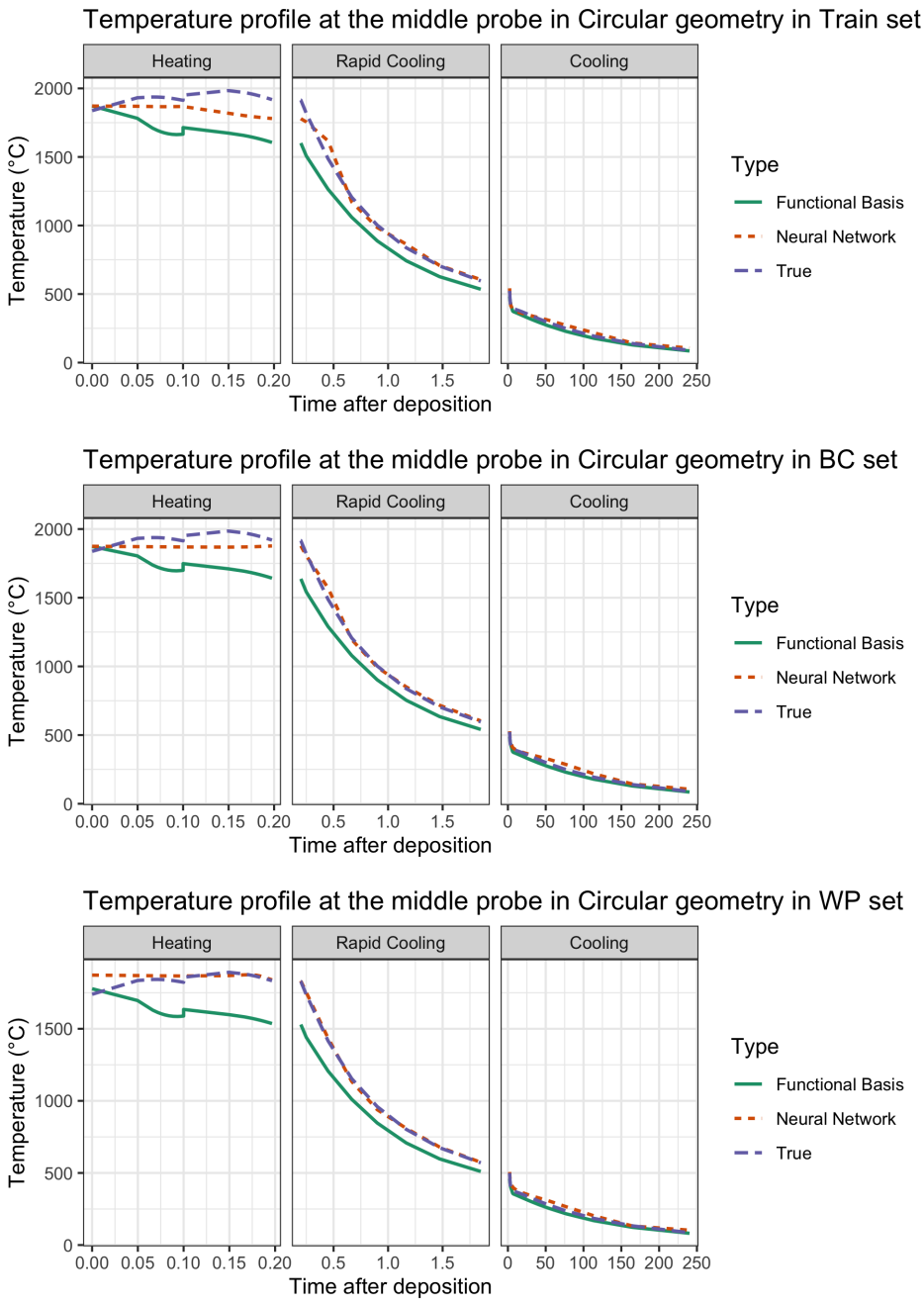

Figure 5.11: Predicted and simulated temperature histories at a middle probe for the circular geometry.

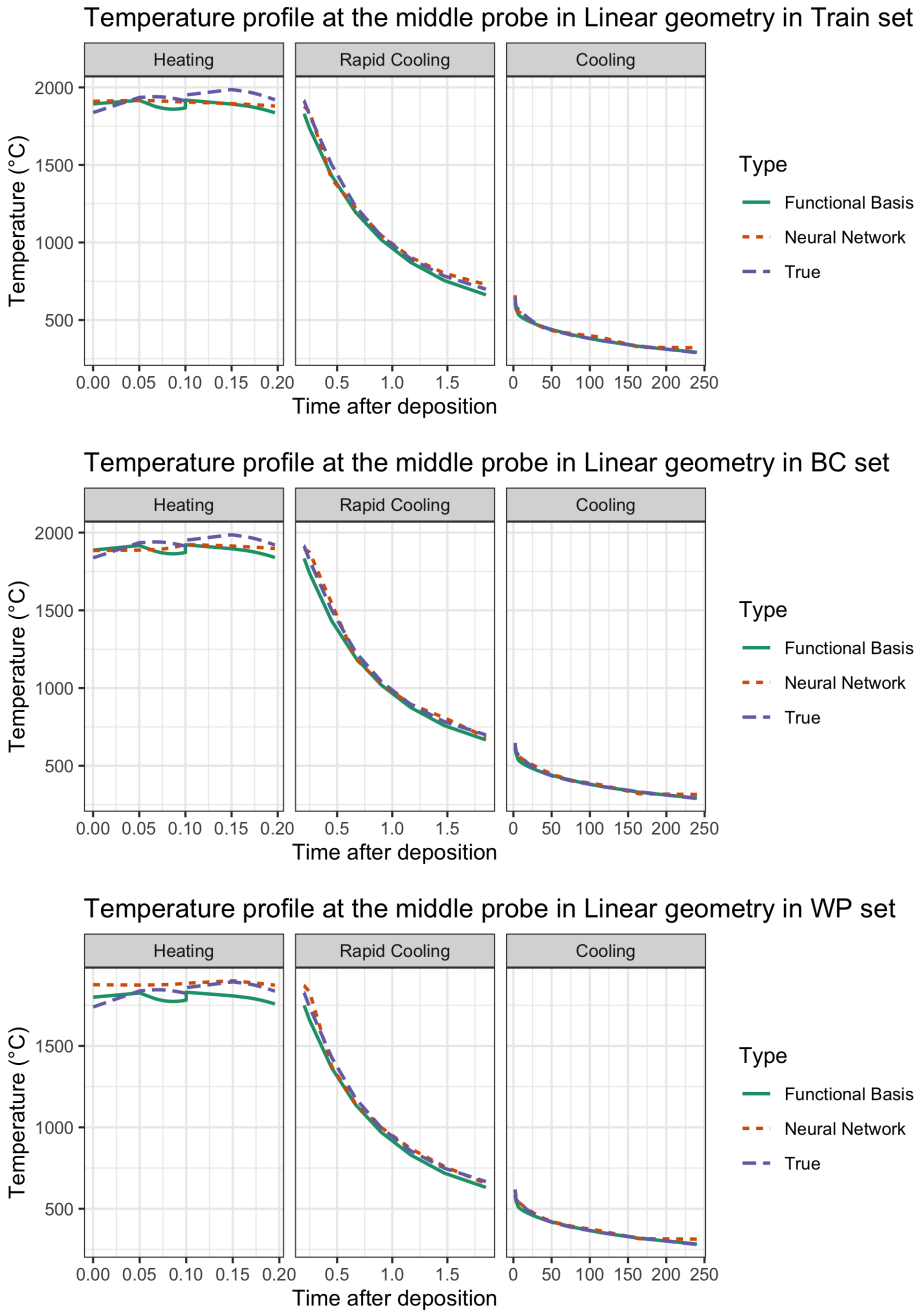

Figure 5.12: Predicted and simulated temperature histories at a middle probe for the linear geometry.

5.9 Limitations

This work has several limitations that should be considered when interpreting the results. First, all surrogate models were trained and validated on ANSYS-generated finite element simulations, without experimental work or infrared measurements. As a result, any systematic modeling bias in the FEM setup is directly inherited by the surrogates. Second, the functional surrogate adopts an additive representation of power in the log–temperature model and relies on a fixed tensor–product basis. While effective within the explored parameter range, this structure may not adequately capture stronger nonlinear interactions that arise under different processing conditions. Finally, the probe layout excluded the bottom cross-section in direct contact with the base plate and emphasized mid-height and upper regions. Consequently, the surrogates do not fully characterize the thermal gradients and substrate–bead interactions near the base plate.

Chapter 6

Conclusions and Future Work

This thesis developed fast surrogate models for predicting temperature histories in single-layer, single-track WAAM. We extended our previous framework to a dense cross-sectional and longitudinal probing, and adding neural network modeling. The functional surrogate represents the logarithm of temperature as a smooth function of time, power, path position, and cross-sectional location, with Gaussian-process–driven coefficients capturing spatial heterogeneity. In parallel, a fully connected neural network surrogate was designed and trained on the same FEM-generated dataset. Across both geometries and test scenarios, the results showed that the surrogates can reproduce high-fidelity ANSYS thermal histories with substantially reduced computational cost. Both models performed well with stable errors, especially in rapid and long-term cooling.

Several extensions follow naturally from these findings. In the present study, travel speed and robot motion were kept fixed; incorporating variable speed, dwell time, and more complex trajectories would allow the surrogates to link kinematics, track shape, and thermal history within a unified framework. The models were also restricted to single-layer, single-track deposition and did not include the bottom cross-section in contact with the base plate, where strong substrate interactions produce markedly different thermal behavior. Future work will extend the surrogates to multi-layer deposition by incorporating prior-layer temperature and build height as additional inputs,

and will explore partitioned spatial domains with boundary-aware Gaussian process parameters to better represent bead–substrate interfaces. Ultimately, integrating these enhanced surrogates with experimental measurements and higher-level models for geometry, microstructure, or residual stress will be an important step toward reliable, simulation-informed planning and control in wire-based MAM.

Chapter B

Probe Generation Script

The following Python script was used to generate probe coordinates across the WAAM half-disk geometry and to automatically create temperature probes in ANSYS using the `ExtAPI` interface.

```
# -*- coding: utf-8 -*-
import math


# ------------------------------------------------------
# 1) Cluster indices to sample
# ------------------------------------------------------
cluster_ids = (
    list(range(0,64))
)


# ------------------------------------------------------
# 2) Angular geometry
# ------------------------------------------------------
n_clusters = 64
cluster_length = 1.25 # mm per cluster arc
deg_per_cluster = 180.0 / n_clusters
rad_per_cluster = math.radians(deg_per_cluster)
```

```
offsets_mm = [0.01, 0.25, 0.50, 0.75, 1.00, 1.25, 0.60, 0.65, 0.70]


def theta_for(cluster_idx, offset_mm):
    theta0 = math.radians((cluster_idx - 1) * deg_per_cluster)
    return theta0 + (offset_mm / cluster_length) * rad_per_cluster


# ------------------------------------------------------
# 3) Crosssection local offsets (13 points per ray)
# ------------------------------------------------------
r_mid = 25.4648 # mm


yz_local = [
    ( 2.2, 10.05), ( 2.2, 11.325), ( 2.2, 12.6),
    (-2.2, 10.05), (-2.2, 11.325), (-2.2, 12.6),
    ( 0.0, 10.05), ( 0.0, 11.325), ( 0.0, 12.6),
    ( 1.1, 10.6875), ( 1.1, 11.9625),
    (-1.1, 10.6875), (-1.1, 11.9625),
]


# ------------------------------------------------------
# 4) Build full list of (x,y,z) coords
# ------------------------------------------------------
probe_coords = []


for cid in cluster_ids:
    for offset in offsets_mm:
        theta = theta_for(cid, offset)
```

```
        c, s = math.cos(theta), math.sin(theta)
        for (y_loc, z) in yz_local:
            r = r_mid + y_loc
            x = r * c
            y = r * s
            probe_coords.append((x, y, z))

# ------------------------------------------------------
# 5) Push into ANSYS
# ------------------------------------------------------
coordinate_systems = ExtAPI.DataModel.Project.Model.CoordinateSystems
analysis = ExtAPI.DataModel.Project.Model.Analyses[0]

for (x, y, z) in probe_coords:
    csys = coordinate_systems.AddCoordinateSystem()
    csys.SetOriginLocation(
        Quantity("%f␣[mm]" % x),
        Quantity("%f␣[mm]" % y),
        Quantity("%f␣[mm]" % z)
    )
    tp = analysis.Solution.AddTemperatureProbe()
    tp.LocationMethod = LocationDefinitionMethod.CoordinateSystem
    tp.CoordinateSystemSelection = csys
    tp.Name = "Probe_%.3f_%.3f_%.3f" % (x, y, z)
    tp.Activate()

# ------------------------------------------------------
```

```
# 6) Summary
# ----------------------------------------------------
total = len(probe_coords)
print("Created␣%d␣probes␣(%d␣clusters␣␣%d␣offsets␣␣%d␣cross-section␣points)"
    %
     (total, len(cluster_ids), len(offsets_mm), len(yz_local)))
```

Reference List

Afazov, S., E. Semerdzhieva, D. Scrimieri, A. Serjouei, B. Kairoshev, and F. Derguti, 2021: An improved distortion compensation approach for additive manufacturing using optically scanned data. *Virtual and Physical Prototyping*, **16 (1)**, 1–13, https://doi.org/10.1080/17452759.2021.1881702, URL https://doi.org/10.1080/17452759.2021.1881702, https://doi.org/10.1080/17452759.2021.1881702.

Akiba, T., S. Sano, T. Yanase, T. Ohta, and M. Koyama, 2019: Optuna: A next-generation hyperparameter optimization framework. *Proceedings of the 25th ACM SIGKDD International Conference on Knowledge Discovery and Data Mining*.

Bai, X., H. Zhang, and G. Wang, 2013: Improving prediction accuracy of thermal analysis for weld-based additive manufacturing by calibrating input parameters using ir imaging. *The International Journal of Advanced Manufacturing Technology*, **69 (5)**, 1087–1095.

Barath Kumar, M., and M. Manikandan, 2022: Assessment of process, parameters, residual stress mitigation, post treatments and finite element analysis simulations of wire arc additive manufacturing technique. *Metals and Materials International*, **28 (1)**, 54–111.

Barik, S., R. Bhandari, and M. K. Mondal, 2024: Optimization of wire arc additive manufacturing process parameters for low-carbon steel and properties prediction by support vector regression model. *steel research international*, **95 (1)**, 2300 369.

Chen, Z., L. Yuan, H. Zhu, D. Ding, H. Li, and Coauthors, 2024: A comprehensive review and future perspectives of simulation approaches in wire arc additive manufacturing (waam). *International Journal of Extreme Manufacturing*, **7 (2)**.

Dashti, A., and C. Ruiz, 2025: Functional models with spatially varying coefficients for fast prediction of temperature history for wire-based metal additive manufacturing. *2025 IEEE 21st International Conference on Automation Science and Engineering (CASE)*, IEEE, 1101–1106.

Dekis, M., M. Tawfik, M. Egiza, and M. Dewidar, 2025: Challenges and developments in wire arc additive manufacturing of steel: A review. *Results in Engineering*, **26**, 104 657, https://doi.org/https://doi.org/10.1016/j.rineng.2025.104657, URL https://www.sciencedirect.com/science/article/pii/S2590123025007340.

Goldak, J., A. Chakravarti, and M. Bibby, 1984: A new finite element model for welding heat sources. *Metallurgical transactions B*, **15**, 299–305.

Irfan, M., Y.-F. Fu, S. Singh, S. U. Butt, A. F. Arif, O. Ibhadode, and A. Qureshi, 2025: Data-driven parameter optimization for bead geometry in wire arc additive manufacturing of 17-4 ph stainless steel. *Journal of Advanced Joining Processes*, **12**, 100 319, https://doi.org/https://doi.org/10.1016/j.jajp.2025.100319, URL https://www.sciencedirect.com/science/article/pii/S2666330925000408.

Jafari, D., T. H. Vaneker, and I. Gibson, 2021: Wire and arc additive manufacturing: Opportunities and challenges to control the quality and accuracy of manufactured parts. *Materials Design*, **202**, 109 471, https://doi.org/https://doi.org/10.1016/j.matdes.2021.109471, URL https://www.sciencedirect.com/science/article/pii/S0264127521000241.

Kammann, E., and M. P. Wand, 2003: Geoadditive models. *Journal of the Royal Statistical Society Series C: Applied Statistics*, **52 (1)**, 1–18.

Lambiase, F., P. Yanala, F. Pace, E. Andreucci, and A. Paoletti, 2025: A state of the art review of wire arc additive manufacturing (waam)–part 1: process fundamentals, parameters and materials. *The International Journal of Advanced Manufacturing Technology*, **138**, 4965–4993, https://doi.org/10.1007/s00170-025-15781-8.

Lin, H., C. Chen, P. Dong, Q. Li, and Y. Yang, 2025: A novel inherent strain method for predicting residual stresses and deformations in metal additive manufacturing. *Computational Mechanics*, 1–17.

Lin, W., C. Ruiz, M. Aroosh, H. Ben-Yoav, and Q. Huang, 2024: Multiresolution functional characterization and correction of biofouling for improved biosensing efficacy. *IISE Transactions*, **56 (6)**, 611–623.

Love, A., O. A. Valdez Pastrana, S. Behseresht, and Y. H. Park, 2025: Advancing metal additive manufacturing: A review of numerical methods in ded, waam, and pbf. *Metrology*, **5 (2)**, 30.

Mattera, G., A. Caggiano, and L. Nele, 2025a: Optimal data-driven control of manufacturing processes using reinforcement learning: an application to wire arc additive manufacturing. *Journal of Intelligent Manufacturing*, **36 (2)**, 1291–1310.

Mattera, G., J. Polden, and L. Nele, 2025b: An efficient data-driven dynamic model for gas metal arc additive manufacturing using ensemble reinforcement learning. *International Journal of Modelling and Simulation*, **0 (0)**, 1–18.

Mondal, S., and S. S. Goswami, 2024: Machine learning techniques for quality assurance in additive manufacturing processes. *International Journal of AI for Materials and Design*, **1 (2)**, 21–40.

Mozaffar, M., A. Paul, R. Al-Bahrani, S. Wolff, A. Choudhary, A. Agrawal, K. Ehmann, and J. Cao, 2018: Data-driven prediction of the high-dimensional thermal history in

directed energy deposition processes via recurrent neural networks. *Manufacturing letters*, **18**, 35–39.

Nalajam, P. K., and R. Varadarajan, 2021: A hybrid deep learning model for layer-wise melt pool temperature forecasting in wire-arc additive manufacturing process. *IEEE Access*, **9**, 100 652–100 664.

Nascimento, E. J., E. dos Santos Magalhães, and L. E. dos Santos Paes, 2023: A literature review in heat source thermal modeling applied to welding and similar processes. *The International Journal of Advanced Manufacturing Technology*, **126 (7)**, 2917–2957.

Norrish, J., J. Polden, and I. Richardson, 2021: A review of wire arc additive manufacturing: development, principles, process physics, implementation and current status. *Journal of Physics D: Applied Physics*, **54 (47)**, 473 001.

Pina, H., and J. Fernandes, 1984: Applications in transient heat conduction. *Basic Principles and Applications*, 41–58.

Ryan, M., M. H. Baqershahi, H. Moshayedi, and E. Ghafoori, 2025: Physics-informed machine learning surrogate for scalable simulation of thermal histories during wire-arc directed energy deposition. *Additive Manufacturing Letters*, 100327.

Sampaio, R., J. Pragana, I. Bragança, C. Silva, C. Nielsen, and P. Martins, 2023: Modelling of wire-arc additive manufacturing–a review. *Advances in Industrial and Manufacturing Engineering*, **6**, 100 121.

Schneider, J., R. Rostami, M. Corcoran, and G. Korpala, 2024: Integration of artificial intelligence into metallography: Area-wide analysis of microstructural components of a jominy sample. *HTM Journal of Heat Treatment and Materials*, **79 (1)**, 3–14.

Schoinochoritis, B., D. Chantzis, and K. Salonitis, 2017: Simulation of metallic powder bed additive manufacturing processes with the finite element method: A critical review. *Proceedings of the Institution of Mechanical Engineers, Part B: Journal of Engineering Manufacture*, **231 (1)**, 96–117.

Singh, S., S. kumar Sharma, and D. W. Rathod, 2021: A review on process planning strategies and challenges of waam. *Materials Today: Proceedings*, **47**, 6564–6575.

Teixeira, P. R. d. F., D. B. d. Araújo, and L. A. B. d. Cunda, 2014: Study of the gaussian distribution heat source model applied to numerical thermal simulations of tig welding processes. *Science & Engineering*, **23 (1)**, 115–122.

Thien, A., N. Van Handel, H. Hu, K. Saleeby, and C. Saldana, 2024: Data efficient modeling for prediction and forecasting of waam process conditions. *International Manufacturing Science and Engineering Conference*, American Society of Mechanical Engineers, Vol. 88100, V001T01A017.

Tian, M., H. Mu, D. Ding, M. Li, Y. Ding, and J. Zhao, 2025: Real-time distortion prediction in metallic additive manufacturing via a physics-informed neural operator approach. *arXiv preprint arXiv:2511.13178*.

Wacker, C., M. Köhler, M. David, F. Aschersleben, F. Gabriel, J. Hensel, K. Dilger, and K. Dröder, 2021: Geometry and distortion prediction of multiple layers for wire arc additive manufacturing with artificial neural networks. *Applied Sciences*, **11 (10)**, https://doi.org/10.3390/app11104694, URL https://www.mdpi.com/2076-3417/11/10/4694.

Wahsh, L., A. ElShater, A. Mansour, F. Hamdy, M. Turky, M. Azzam, and H. Salem, 2018: Parameter selection for wire arc additive manufacturing (waam) process. *Mater. Sci. Technol*, 78–85.

Watanabe, S., 2023: Tree-structured parzen estimator: Understanding its algorithm components and their roles for better empirical performance. *arXiv preprint arXiv:2304.11127*.

Wendland, H., 1998: Error estimates for interpolation by compactly supported radial basis functions of minimal degree. *Journal of approximation theory*, **93 (2)**, 258–272.

Wood, S., 2017: *Generalized Additive Models: An Introduction with R*. 2nd ed., CRC Press, United States.

Xia, C., Z. Pan, J. Polden, H. Li, Y. Xu, S. Chen, and Y. Zhang, 2020: A review on wire arc additive manufacturing: Monitoring, control and a framework of automated system. *Journal of manufacturing systems*, **57**, 31–45.

Xiong, J., Y. Lei, and R. Li, 2017: Finite element analysis and experimental validation of thermal behavior for thin-walled parts in gmaw-based additive manufacturing with various substrate preheating temperatures. *Applied Thermal Engineering*, **126**, 43–52.

Yan, Z., W. Liu, Z. Tang, X. Liu, N. Zhang, M. Li, and H. Zhang, 2018: Review on thermal analysis in laser-based additive manufacturing. *Optics & Laser Technology*, **106**, 427–441.

Zhang, H., and Coauthors, 2024: State-of-art review on the process-structure-properties-performance linkage in wire arc additive manufacturing. *Virtual and Physical Prototyping*, **19 (1)**, e2390 495.

Zhou, Z., H. Shen, B. Liu, W. Du, and J. Jin, 2021: Thermal field prediction for welding paths in multi-layer gas metal arc welding-based additive manufacturing: A machine learning approach. *Journal of Manufacturing Processes*, **64**, 960–971.